Manuscript File Click here to view linked References

Unusual Stress and Strain Concentration Behaviors at the Circular Hole of a Large Monodomain Liquid Crystal Elastomer Sheet

Yuefeng Jiang[a], Lihua Jin[b,*], Yongzhong Huo[a,*]

[a] Institute of Mechanics and Computational Engineering, Department of Aeronautics and Astronautics, Fudan University, Shanghai, 200433, China

[b] Department of Mechanical and Aerospace Engineering, University of California, Los Angeles, CA 90095, USA

*Corresponding authors: lihuajin@seas.ucla.edu, yzhuo@fudan.edu.cn

Abstract

Liquid crystal elastomers combine the hyperelasticity of elastomers with the multi-functionality of liquid crystals and have emerged as an important class of soft active materials. Monodomain liquid crystal elastomers under loading exhibit the soft elastic behavior due to the stress induced director rotation and the resulting spontaneous strain. Here, we numerically study their stress and strain concentration behavior by considering the classical example, a large sheet with a small circular hole in the middle under uniaxial loading. The concentration behavior is found to be very different from regular elastomers. Firstly, the concentration factors are much bigger at both small and large strains. Secondly, the locations of the strain concentration may not coincide with that of the stress concentration. Detailed analysis of the director rotation and the resulting spontaneous strain around the free edge of the hole are shown to be the main causes for the unusual concentration behavior. Moreover, under a given strain, the stress level of the LCE sample, and therefore the free energy, is slightly lower than that of the neo-Hookean material, while the local free energy density on the hole edge is much bigger due to the severer concentrations. By

considering material parameters obtained from various samples of polysiloxane and polyacrylate side-chain nematic elastomers, we find that their stress and strain concentration behaviors are qualitatively similar but quantitatively quite different. As a result, at a prescribed strain, the samples with a larger maximal spontaneous strain has severer stress and strain concentrations. The stress concentration factor difference scaled by a coupling constant that combines the effect of the two material parameters, r and a, increases as the semi-soft coefficient a decreases. Similar results are found for the scaled maximal spontaneous strains and the scaled strain concentration factor difference at small strains.

Keywords: liquid crystal elastomers; director rotation; semi-soft elasticity; stress concentration; strain concentration; finite element method

1. Introduction

Liquid crystal elastomers (LCEs) are prepared by integrating mesogenic molecules into a polymer network. These materials hence show a combination of large elastic deformability and the properties of liquid crystals (LCs) (Warner and Terentjev, 2007). Because of the LC mesogens, LCEs can generate large elastic deformations in response to multiple stimuli, like light illumination (Camacho-Lopez et al., 2004; Finkelmann et al., 2001b), heating (Kuenstler et al., 2020; Sawa et al., 2010), and electromagnetic fields (Davidson et al., 2019; Fukunaga et al., 2008; Zentel, 1986). These material properties provide LCEs a variety of potential applications such as artificial muscle (Thomsen et al., 2001; Wang et al., 2017; Woltman et al., 2007) and mechanically tunable optical devices (Gebhart et al., 2007; Schuhladen et al., 2014; Xing et al., 2016).

Both the order and the orientation of the LC mesogens can affect the mechanical properties of LCEs visibly. The change of the order, which is usually induced by heat or light, can generate significant spontaneous strain and produce a macroscopic deformation (Finkelmann et al., 2001b; Tajbakhsh and Terentjev, 2001). The average

orientation of LC mesogens is defined as the director. LCEs exhibit anisotropic mechanical behaviors associated with the director, and the degree of anisotropy is affected by the order significantly (Finkelmann et al., 2001a; Hirschmann et al., 2001). The director can rotate gradually in response to the overall deformations, which leads to a soft elastic behavior, resulting in a stress plateau at a very low stress value in the stress-strain curve (Dey et al., 2013; Higaki et al., 2013; Kundler and Finkelmann, 1995; Mitchell et al., 1993). The rotation can be either uniform (Higaki et al., 2013) or non-uniform with stripe-domains (Kundler and Finkelmann, 1995). On the other hand, discontinuous rotations have also been reported by Mitchell et al. (Mitchell et al., 1993). The soft elasticity can be captured by the neo-classical model (Bladon et al., 1993; He et al., 2020; Jin et al., 2010; Warner, 1999; Warner and Terentjev, 1996). When monodomain LCEs are crosslinked in the nematic phase, they usually show semi-soft elasticity, i.e. the stress plateaus at a relatively high value in the stress-strain curve (Küpfer and Finkelmann, 1994). Considering possible compositional fluctuations, Verwey et al. proposed a semi-soft elastic energy (Verwey and Warner, 1995, 1997; Verwey et al., 1996), which has been successfully applied to model the stripe instability (Conti, 2002; Conti et al., 2002; Finkelmann et al., 1997; Plucinsky and Bhattacharya, 2017; Zhang et al., 2020) and other complex deformations related to the stress induced director rotations (Biggins et al., 2008; Warner and Terentjev, 2007; Zhang et al., 2019).

Many applications of LCEs are based on their mechanical behaviors under high stress or strain. Although there are a lot of discussions about the soft-elasticity in flawless samples, the possible effects of an initial flaw in a sample are not clear yet. Some primary experimental studies (Fan et al., 2016) revealed that the fracture behaviors of monodomain and polydomain LCEs are quite different from common elastomers. The fracture energy is significantly affected by the orientation and the order of LC mesogens. Besides, a remarkable director rotation is clearly observed within the vicinity of the crack-tip. As a step before failure, the stress and strain concentration

behavior of LCEs is an important subject to study.

High local stress and strain concentrate nearby geometric defects such as holes, notches and cracks, where failures start (Elmukashfi and Kroon, 2014). For linear elastic materials, the asymptotic stress/strain fields near a hole, notch and crack have been solved analytically in the literature (Fowler, 1984; Qian and Gao, 2001; Walter and Deborah, 2007; Wong and Shield, 1969). Numerical simulations and experimental approaches have also been carried out to obtain the stress and strain fields (Gomes et al., 2005; Heydari-Meybodi et al., 2018; Legrain et al., 2005; Livne et al., 2008; Troyani et al., 2002). The stress concentration factor is often utilized to describe the amplification of stress at defects and is very useful for engineering applications (Walter and Deborah, 2007). Similarly, the strain concentration at defects can be considered. Yang et al realized that the location of strain concentration can differ from that of the stress concentration in an elastic plate of finite thickness (Yang, 2009; Yang et al., 2008).

For elastomers with nonlinear elasticity, there have been some attempts to analyze the stress/strain distribution and concentration around a circular hole through analytical approaches (Rivlin and Thomas, 1951; Yang, 1967). Some experimental techniques have also been developed to obtain the stress/strain distribution (Larocca et al., 2004; Spagnoli et al., 2019). Numerical simulations based on the finite element method have become reliable approaches to study the concentration behavior of nonlinear materials (Fukahori and Seki, 1993b, a; Khajehsaeid et al., 2016; Lindley, 1971, 2007; Troyani, 2003; Tsui et al., 2001; Wang and Lee, 1999). It is found that the stress and strain concentrations of hyperelastic materials behave the same as linear Hooke materials at very small strains, but can differ strongly at large loadings. The strain-dependent stress and strain concentration factors are affected greatly by the hyperelastic models and the material constants (Fukahori and Seki, 1993b, a; Khajehsaeid et al., 2016). As the mechanical behavior of nematic elastomers differs strongly from the regular rubbers due to the stress induced director rotation, we would also expect very different stress

and strain concentration behaviors.

In this article, we shall consider the classical example of stress and strain concentrations, namely, a large thin sheet with a small circular hole in the middle under uniaxial loading. Analytical solutions of the stress and strain fields are known for linear Hook materials. Numerical solutions are available for various hyperelastic materials. Nevertheless, our numerical simulations have shown that the concentration behavior of nematic elastomers is indeed very different in many aspects, e.g. the values of the concentration factors, locations of the concentrations and so on. We use the continuum mechanical model (Zhang et al., 2019) and the semi-soft elastic energy (Verwey and Warner, 1997) to carry out the numerical simulations based on the finite element methods as will be described briefly in Section 2. A monodomain LCE sample in the deep nematic state is studied in details in Section 3. We analyze the stress and strain concentration behavior by considering the director rotation and the spontaneous strain around the circular hole. In Section 4, the material-dependent concentration behavior is studied by using material constants obtained from various experiments of side-chain LCEs reported in the literature. The conclusions are given in Section 5.

2. Continuum Mechanical Model and Numerical Method

In this section, we shall list the balance and constitutive equations in the continuum mechanical model of LCE (Zhang et al., 2019). Then, the semi-soft elastic energy and the corresponding stress-strain relation are provided. Afterwards, we shall derive the governing equations for plane problems and describe the numerical method for our calculations.

2.1 Balance and constitutive equations

LCEs have rod-like liquid crystal mesogens and their average orientation is defined as the director, $\mathbf{d}$, which is a unit vector. According to the Lagrangian

description of the motion, $\boldsymbol{x}(\mathbf{X},t)$ gives us the current position $\boldsymbol{x}$ in the current configuration $B_t(\boldsymbol{x}\in B_t)$ of a particle that occupied position $\mathbf{X}$ in the initial configuration $B_0(\mathbf{X}\in B_0)$. The director filed in the current and the initial configuration are defined as the $\mathbf{d}_0(\mathbf{X})$ and $\mathbf{d}(\boldsymbol{x},t)$, respectively. Thus, the free energy density of the nematic LCEs should depend on the deformation gradient $\mathbf{F}:=\nabla_X\boldsymbol{x}$, the director, and its gradient $\nabla\mathbf{d}$ as

$$f=f(\mathbf{F},\mathbf{d},\nabla\mathbf{d},\mathbf{d}_0) \tag{1}$$

where ∇ is the gradient operator with respect to $\boldsymbol{x}$.

To consider the bulk viscosity and the dissipative rotation of the director, a Rayleigh dissipation density function should be given as

$$R=R\left(\dot{\boldsymbol{\varepsilon}},\overset{\circ}{\mathbf{d}},\mathbf{F},\mathbf{d},\mathbf{d}_0\right) \tag{2}$$

where $\dot{\boldsymbol{\varepsilon}}=\left(\nabla_x\dot{\mathbf{u}}+\nabla_x\dot{\mathbf{u}}^T\right)/2$ is the strain rate tensor, and $\overset{\circ}{\mathbf{d}}=\dot{\mathbf{d}}-\mathbf{W}\mathbf{d}$ is the Jaumann derivative. $\dot{\mathbf{u}}$ and $\dot{\mathbf{d}}$ are the material derivatives of the displacement field $\mathbf{u}(\boldsymbol{x},t)$ and the director field $\mathbf{d}(\boldsymbol{x},t)$, respectively. $\mathbf{W}=\left(\nabla_x\dot{\mathbf{u}}-\nabla_x\dot{\mathbf{u}}^T\right)/2$ is the spin tensor.

A continuum mechanical model was proposed for nematic LCEs (Zhang et al., 2019). Based on the variational principle, the balance equations for the momentum and the director rotation have been obtained. Namely, neglecting the inertia effect, the stress equilibrium reads

$$\nabla\cdot\mathbf{t}=\mathbf{0}\ \text{ in }\ B_t\ \text{ and }\ \mathbf{t}\cdot\mathbf{n}=\mathbf{t}_n\ \text{ at }\ S_t\subset\partial B_t \tag{3}$$

where $\mathbf{t}$ is the Cauchy stress tensor, and $\mathbf{n}$ is the outer normal at the traction boundary $S_t\subset\partial B_t$ with $\mathbf{t}_n$ the prescribed stress.

The governing equation for the director field $\mathbf{d}(\boldsymbol{x},t)$ is

$$\mathbf{g}+\nabla\cdot\boldsymbol{\pi}=\gamma\mathbf{d}\ \text{ in }\ B_t\ \text{ and }\ \boldsymbol{\pi}\cdot\mathbf{n}=\mathbf{C}_n\ \text{ at }\ S_d\subset\partial B_t \tag{4}$$

where $\boldsymbol{\pi}$ is the generalized surface stress tensor, $\mathbf{g}$ is the generalized intrinsic body force, γ is a Lagrange multiplier for the constraint, $\|\mathbf{d}\|=1$, and $\mathbf{C}_n$ is the prescribed

generalized surface stress.

The constitutive equations for Cauchy stress $\mathbf{t}$ is derived as

$$\mathbf{t} = \mathbf{t}^{bulk} + \mathbf{t}^{Ericksen} + \mathbf{t}^{Leslie} \tag{5}$$

with the bulk and director elastic parts as

$$\mathbf{t}^{bulk} = -p\mathbf{I} + \frac{\partial f}{\partial \mathbf{F}}\mathbf{F}^T \quad \text{and} \quad \mathbf{t}^{\text{Ericksen}} = -(\nabla \mathbf{d})^T \frac{\partial f}{\partial \nabla \mathbf{d}} \tag{6}$$

where p is a Lagrange multiplier to deal with the incompressibility, and the viscous part from the dissipations of the bulk deformations and the director rotations as

$$\mathbf{t}^{Leslie} = \frac{\partial R}{\partial \dot{\boldsymbol{\varepsilon}}} + \frac{1}{2}\left(\mathbf{d} \otimes \frac{\partial R}{\partial \overset{\circ}{\mathbf{d}}} - \frac{\partial R}{\partial \overset{\circ}{\mathbf{d}}} \otimes \mathbf{d} \right) \tag{7}$$

The generalized stress and body force, $\boldsymbol{\pi}$ and $\mathbf{g}$, are given as

$$\boldsymbol{\pi} = \frac{\partial f}{\partial \nabla \mathbf{d}} \quad \text{and} \quad \mathbf{g} = -\frac{\partial f}{\partial \mathbf{d}} - \frac{\partial R}{\partial \overset{\circ}{\mathbf{d}}} \tag{8}$$

According to the above model, once we have the two constitutive functions, the free energy density f of (1) and Rayleigh dissipation density R of (2), the current position of material points $\boldsymbol{x}(\mathbf{X},t)$ and the current director $\mathbf{d}(\boldsymbol{x},t)$ can be calculated through (3) and (4) for LCE samples with any given initial director field $\mathbf{d}_0(\mathbf{X})$ at B_0. In the following, we shall use the semi-soft elastic energy for LCEs (Verwey and Warner, 1997), the one-constant Frank energy for LCs (de Gennes and Prost, 1994), and the two-constant Rayleigh function used (Zhang et al., 2019). More sophistical expressions are discussed by Zhang et al. (Zhang et al., 2019).

2.2 Semi-soft elasticity and spontaneous strains

We assume that the free energy density (1) can be decomposed into the bulk elastic and the Frank energy as

$$f = f_{elastic} + f_{Frank} \tag{9}$$

where the bulk elastic energy f_{elast} depends on the deformation gradient $\mathbf{F}$, the director $\mathbf{d}_0(\mathbf{X})$ at the initial configuration and $\mathbf{d}(\boldsymbol{x},t)$ at the current configuration. The Franke energy is related to the spatially inhomogeneous distribution of the director field $\mathbf{d}(\boldsymbol{x},t)$ (de Gennes and Prost, 1994). For simplicity, we assume one constant approximation of the Frank coefficient $K>0$ as

$$f_{Frank}=\frac{1}{2}K\nabla\mathbf{d}:\nabla\mathbf{d} \tag{10}$$

where ":" is the inner product of two second order tensors. Thus by (6) and (10), the Ericksen stress are

$$t_{ij}^{\text{Ericksen}}=-Kd_{k,i}d_{k,j} \tag{11}$$

It is obvious that the Ericksen stress is symmetric.

The semi-soft elastic energy f_{elast} (Verwey and Warner, 1997) is,

$$f_{elast}=\frac{\mu}{2}\left(\text{tr}\left(\ell^{-1}\mathbf{F}\ell_0\mathbf{F}^T\right)+a\text{tr}\left(\mathbf{d}\otimes\mathbf{d}\cdot\mathbf{F}\left(\mathbf{I}-\mathbf{d}_0\otimes\mathbf{d}_0\right)\mathbf{F}^T\right)\right) \tag{12}$$

where $\mu>0$ is the shear modulus and $a\geq 0$ is the semi-soft coefficient. ℓ_0 and ℓ are the reduced shape tensors of a LCE at the initial and the current configurations, respectively. They are given as

$$\ell_0=(r-1)\mathbf{d}_0\otimes\mathbf{d}_0+\mathbf{I} \quad \text{and} \quad \ell=(r-1)\mathbf{d}\otimes\mathbf{d}+\mathbf{I} \tag{13}$$

where $\mathbf{I}$ is a unit tensor and $r>0$ is the step length ratio (SLR) as shown in Fig. 1(a). r denotes the average shape anisotropy of the Gaussian distribution of network chains. When r =1 and a = 0, the LCE is in the isotropic phase and (12) recovers the well-known neo-Hookean elastic energy of rubbers In the nematic phase, $r>1$ corresponds to prolate LCEs and $0<r<1$ corresponds to oblate LCEs. If $r\neq 1$ but $a=0$, we have the neo-classical elastic energy of LCEs (Bladon et al., 1993). It predicts the soft behavior under loading. Namely, the director will rotate to align itself to the

loading axis under a negligibly small stress (Warner, 1999) as schematically shown in Fig. 1(a). For the monodomain LCE samples considered in our work, there is a critical driving force to rotate the director due to the restriction from the backbone polymer network, and are therefore modeled by the semi-soft elastic energy with a small but positive semi-soft coefficient $a>0$. We can rewrite the elastic energy (12) into the following form

$$f_{elast}=\frac{\mu}{2}\left(\mathrm{tr}\left(\mathbf{F}_e\mathbf{F}_e^T\right)+a\left\|\mathbf{d}_F\right\|^2\right) \tag{14}$$

where $\mathbf{F}_e:=\ell^{-1/2}\mathbf{F}\ell_0^{1/2}$ can be considered as the elastic part of the deformation gradient (Jin et al., 2010). $\mathbf{d}_F:=\mathbf{F}^T\mathbf{d}-\left(\mathbf{F}^T\mathbf{d}\cdot\mathbf{d}_0\right)\mathbf{d}_0$ represents the deviation of $\mathbf{F}^T\mathbf{d}$ from its initial alignment $\mathbf{d}_0$ as indicated in Fig. 1(b). Thus, we know from (14) that the director rotation towards the loading axis is favored by the first term as it can reduce this neo-classical energy, but is penalized by the semi-soft energy as it vanishes only when $\mathbf{F}^T\mathbf{d}$ remains parallel to $\mathbf{d}_0$.

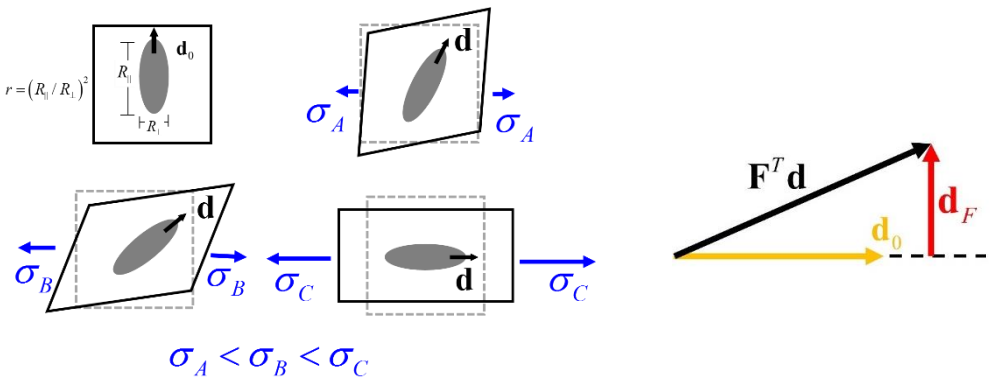

(a) (b)

Fig. 1. Schematics for soft elasticity and semi-softness. (a) Stress induced director rotation and spontaneous strains. The gyration tensor spheroids and the director (black arrow) are plotted for reference. $R_{//,\perp}$ is the radius of gyration parallel and perpendicular to the director $\mathbf{d}$, respectively. The step length ratio $r=\left(R_{\parallel}/R_{\perp}\right)^2$ represents the chain anisotropy of the backbone molecules (Warner and Terentjev, 2007). For prolate LCEs ($r>1$), the director will immediately rotate toward the loading direction (soft behavior). (b) The semi-soft energy penalizes director

rotations and attains the minimum at $\mathbf{d}_F = \mathbf{0}$, i.e. when $\mathbf{F}^T\mathbf{d}$ is parallel to $\mathbf{d}_0$.

Now inserting (13) into (12) and using (6), we have the bulk elastic stress as

$$\mathbf{t}^{bulk} := -p\mathbf{I} + \frac{\partial f_{elastic}}{\partial \mathbf{F}}\mathbf{F}^T = -p\mathbf{I} + \mu\left(\mathbf{B} - \mathbf{B}^{LCE}\right) \tag{15}$$

where $\mathbf{B} := \mathbf{F}\mathbf{F}^T$ is the left Cauchy-Green tensor and $\mathbf{B}^{LCE}$ is given by

$$\mathbf{B}^{LCE} := \mathbf{d} \otimes \hat{\mathbf{g}}^b - (r-1)\mathbf{F}\mathbf{d}_0 \otimes \mathbf{F}\mathbf{d}_0 \tag{16}$$

with $\hat{\mathbf{g}}^b$ defined as

$$\hat{\mathbf{g}}^b := r^{-1}(r-1-ra)\mathbf{B}\mathbf{d} + r^{-1}\left((r-1)^2 + ra\right)(\mathbf{F}\mathbf{d}_0 \cdot \mathbf{d})\mathbf{F}\mathbf{d}_0 \tag{17}$$

It is obvious that the bulk elastic stress tensor (15) is generally not symmetric. Its symmetric part, denoted as $\boldsymbol{\sigma}^{bulk}$ is

$$\boldsymbol{\sigma}^{bulk} = -p\mathbf{I} + \mu\left(\mathbf{B} - \mathbf{B}^s\right) \tag{18}$$

where $\mathbf{B}^s$ is obtained by (16) as

$$\mathbf{B}^s := \frac{1}{2}\left(\mathbf{d} \otimes \hat{\mathbf{g}}^b + \hat{\mathbf{g}}^b \otimes \mathbf{d}\right) - (r-1)\mathbf{F}\mathbf{d}_0 \otimes \mathbf{F}\mathbf{d}_0 \tag{19}$$

and can be considered as the spontaneous strain. The skew-symmetric part $\boldsymbol{\tau}^{bulk}$ of the bulk stress (15) is

$$\boldsymbol{\tau}^{bulk} = \frac{\mu}{2}(\hat{\mathbf{g}}^b \otimes \mathbf{d} - \mathbf{d} \otimes \hat{\mathbf{g}}^b) \tag{20}$$

The viscosity of the bulk and the viscosity of the rotation of the director are taken into consideration here. The form of the dissipation density function is given as:

$$R = \frac{1}{2}\eta_b \mathrm{tr}\left(\dot{\boldsymbol{\varepsilon}}^2\right) + \frac{1}{2}\eta_d \left\| \overset{\circ}{\mathbf{d}} \right\|^2 \tag{21}$$

where η_b is the coefficient of the bulk viscosity and η_d is the coefficient of the

viscosity of the director rotation.

Inserting (21) into (7), we can obtain the Leslie stress as

$$\mathbf{t}^{Leslie}=\boldsymbol{\sigma}^{Leslie}+\boldsymbol{\tau}^{Leslie}\quad\text{with}\quad\boldsymbol{\sigma}^{Leslie}=\eta_b\dot{\boldsymbol{\varepsilon}}\quad\text{and}\quad\boldsymbol{\tau}^{Leslie}=\frac{\eta_d}{2}\left(\mathbf{d}\otimes\overset{\circ}{\mathbf{d}}-\overset{\circ}{\mathbf{d}}\otimes\mathbf{d}\right)\tag{22}$$

where $\boldsymbol{\sigma}^{Leslie}$ and $\boldsymbol{\tau}^{Leslie}$ are the symmetric and skew-symmetric parts, respectively.

Thus, (3) and (4) are the governing equations for the displacement $\mathbf{u}(\mathbf{X},t)$ and the director field $\mathbf{d}(\boldsymbol{x},t)$. To reduce the rather high computation cost, we shall consider only plane problems in the following.

2.3 The plane problem

We consider a thin monodomain LCE sheet with an in-plane initial director $\mathbf{d}_0$ as shown in Fig. 2(a). Considering only in-plane loadings and using the rectangular coordinate system (x,y) in Fig. 2(b), we can assume that the out of plane stress components all vanish, i.e. $t_{xz}=t_{zx}=t_{yz}=t_{zy}=t_{zz}\equiv 0$ and the director fields remain in the x-y plane,

$$\mathbf{d}_0=\left(\cos\theta_0,\sin\theta_0,0\right)^T\quad\text{and}\quad\mathbf{d}=\left(\cos\theta,\sin\theta,0\right)^T\tag{23}$$

with $\theta_0=\text{constant}$ and θ the initial and current angles of the directors with respect to the x axis, respectively. The director field θ and the in-plane displacement u, v are functions of (x,y,t) at the current configuration or (X,Y,t) at the initial configuration.

The stress equilibrium equation (3) is reduced to two equations as

$$t_{xx,x}+t_{xy,y}=0\quad\text{and}\quad t_{yx,x}+t_{yy,y}=0\tag{24}$$

By (20) and (22), the skew-symmetric stress $\tau_{yx}=\tau_{yx}^{bulk}+\tau_{yx}^{Leslie}$ is

$$2\tau_{yx}^{bulk}=\mu\left(\hat{g}_y^b\cos\theta-\hat{g}_x^b\sin\theta\right)\quad\text{and}\quad2\tau_{yx}^{Leslie}=\eta_d\left(-\dot{\theta}+W_{yx}\right)\tag{25}$$

where $\hat{g}_x^b$ and $\hat{g}_y^b$ are the in-plane components of the vector $\hat{\mathbf{g}}^b$ of (17), and W_{yx}

is the y-x component of the skew-symmetric spin tensor **W**.

To avoid the unknown Lagrange multiplier γ in (4) and consider the plane stress problem that we studied here, Zhang et al. has derived the following rotational momentum balance equation as (Zhang et al., 2019)

$$\eta_d\left(\dot{\theta}-W_{yx}\right)-K\nabla^2\theta=2\tau_{yx}^{bulk} \tag{26}$$

The skew-symmetric stress component acts as the driving force for the director rotation. The boundary condition of the director field is considered to be free, i.e. $\nabla\theta\cdot\mathbf{n}=0$ with $\mathbf{n}$ the outer normal at the boundaries.

The three equations (24) and (26) can be solved by using the finite element method (FEM) to obtain the three unknown fields u, v and θ, as will be discussed in details in the next subsection.

2.4 FEM simulations and mesh generations

We use the commercial FEM software COMSOL Multiphysics to solve the above plane problem (24) and (26). The Structure Mechanics Module is implemented for the stress equilibrium (24) together with the Mathematics Module for (26). The total Lagrangian scheme is chosen for large deformations. Namely, the two displacements $u(X,Y,t)$, $v(X,Y,t)$ and the director field $\theta(X,Y,t)$ will be determined at the initial configuration.

As shown in Fig. 2(a), we consider a square shaped monodomain LCE sample of length $2L_0$ with a very small circular hole of diameter $2\rho_0 << 2L_0$ in the middle. To achieve a uniaxial loading condition, we assume that the sample is free on the top and the bottom. On the left and right sides, the displacements are prescribed as,

$$u(\pm L_0,Y,t)=\pm L_0(\lambda-1) \quad \text{and} \quad v(-L_0,0,t)=0 \tag{27}$$

where $\lambda:=1+\dot{\lambda}t$ is the stretch with $\dot{\lambda}>0$ a constant stretching rate and the last condition is given to prevent any rigid motions. By the penalty function method, we set

the hydrostatic pressure in (6) as $p=\kappa_p\left(\det(\mathbf{F})-1\right)$ to deal with the incompressibility. The penalty factor κ_p/μ is large enough to give sufficient precision.

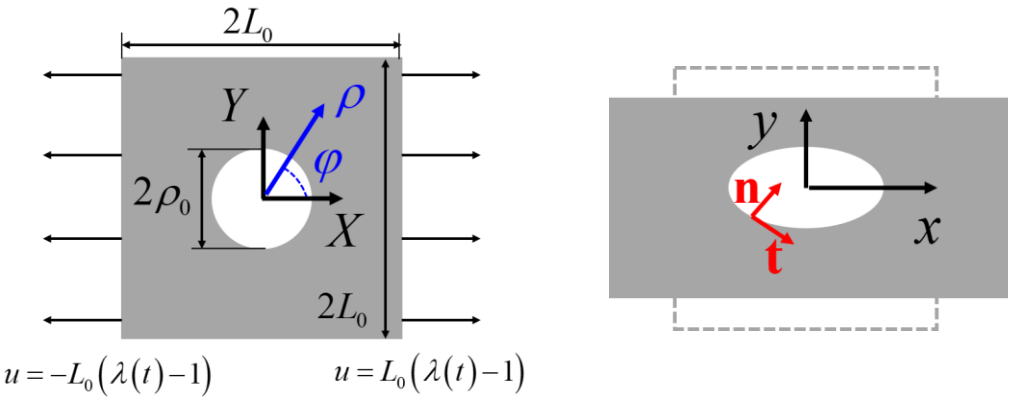

(a) (b)

Fig. 2 Schematic of a square LCE sheet of length $2L_0$ with a center small circular hole of radius ρ_0 under uniaxial loading. The initial director $\mathbf{d}_0$ and the loading are both parallel to the X-axis. (a) the sample at the initial configuration with the coordinate (X,Y) and (ρ,φ); (b) the sample at the current configuration with the coordinate (x,y). $\mathbf{n}$ and $\mathbf{t}$ are the normal vector and the tangent vector on the hole edge, respectively. (X,Y) coincides with (x,y) at the beginning.

We consider a prolate monodomain LCE sample with the step length ratio $r>1$. For side-chain nematic elastomers in the deep nematic phase, we adopt the material parameters determined in some previous studies (Zhang et al., 2019).

$$\mu=10^5\ Pa,\ K=10^{-11}\ N,\ \eta_b=10\ Pa\cdot s,\ \eta_d=10^3\ Pa\cdot s \tag{28}$$

The initial, geometric and loading parameters are chosen as

$$\theta_0=0^\circ,\ 2L_0=15mm,\ 2\rho_0=0.3mm,\ \dot{\lambda}=10^{-9}s^{-1} \tag{29}$$

From (28), there are two characteristic times $t_b=\eta_b/\mu=10^{-4}s$ for the bulk viscosity and $t_d=\eta_d/\mu=10^{-2}s$ for the dissipation due to director rotations. Thus, with the loading rate of (29), the effects of viscosity are negligible, as $\dot{\lambda}t_b=10^{-13}\ll 1$

and $\dot{\lambda} t_d = 10^{-11} \ll 1$. The loading process can be regarded as quasi-static. Possible rate dependence of the stress/strain concentration behavior will be studied in some future work. Moreover, the very small coefficient K indicates that the contribution of the Frank energy may also be negligible compared to that of the semi-soft elasticity, which is confirmed by the following results. The rotational momentum balance equation (26) actually reflects $\tau_{yx}^{bulk} = 0$ at every relaxed step. In other words, the director rotates to eliminate the skew-symmetric stress induced by the semi-soft elasticity.

We have $\rho_0 / L_0 = 1/50$ by (29). The circular hole is designed small enough to wipe off the boundary effects of the square sheet, so the sample can be regarded as nearly infinite. We therefore introduce the analytical solution of an infinite-size plate of linear Hooke materials to make relevant comparisons at the small strain case. (Walter and Deborah, 2007)

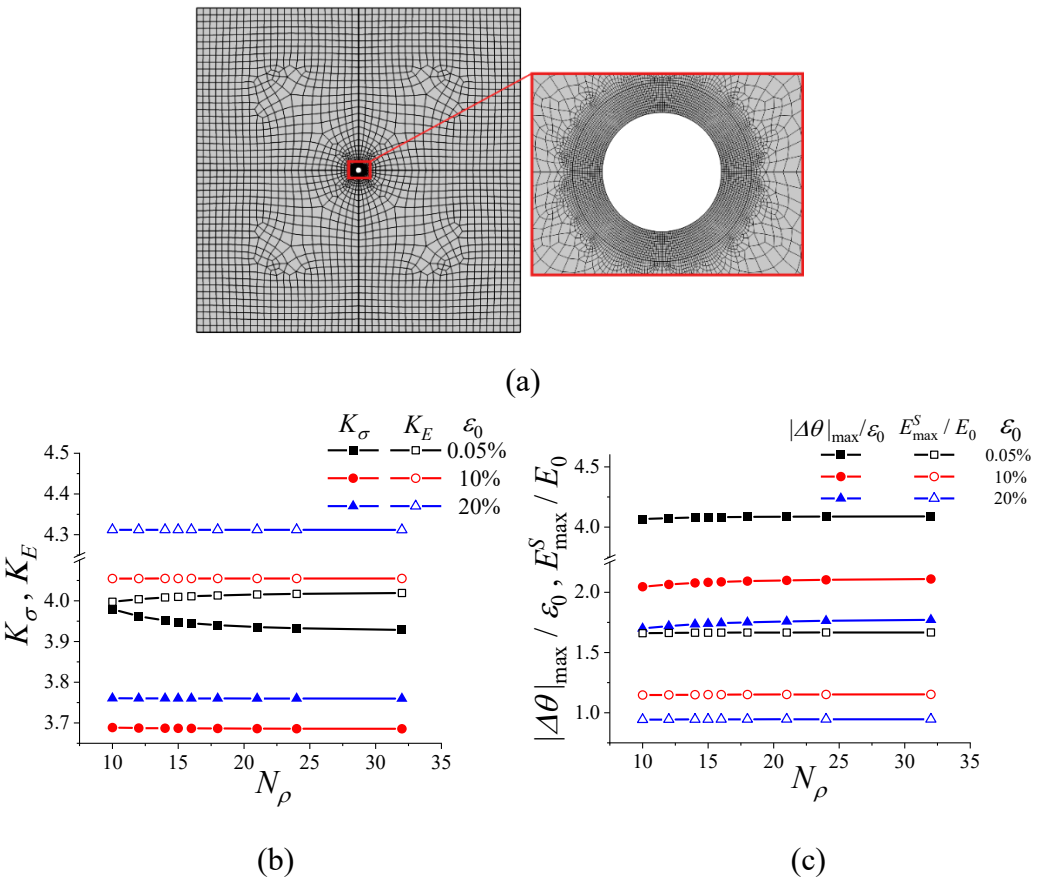

Fig. 3. The mesh and its convergence. (a) The mesh generated using the quadrilateral elements

with refinement at the hole edge. The circular ring $\rho_0 \le \rho \le 1.5\rho_0$ is meshed by $N_\varphi \times N_\rho$ quadrilateral elements with N_φ and N_ρ the number of elements in the circumferential and the radial direction, respectively. (b) Convergence of the maxima of the stress concentration factor K_σ and the strain concentration factor K_E. (c) Convergence of the maximal director rotation $|\Delta\theta|_{\max}$ and the maximal principal spontaneous strain $E^S_{\max}$ with the increase of N_ρ.

Considering a sample in the deep nematic state with $r = 1.8$, $a = 0.1$, Fig. 3(a) depicts an example of the mesh generated using the quadrilateral elements. The mesh around the hole edge was refined in order to study the stress/strain concentrations. Namely, the small circular region around the hole edge ($\rho_0 \le \rho \le 1.5\rho_0$) is meshed by $N_\varphi \times N_\rho$ quadrilateral elements, with N_φ and N_ρ the numbers of elements in the circumferential and radial direction, respectively, and $N_\varphi = 20N_\rho$. Then, we mesh the outer edge of the sample by $4N_L$ quadrilateral elements. A rather coarse mesh is used here with $N_L = 6N_\rho$. In between, the mesh with quadrilateral elements is generated automatically by COMSOL with the maximal element size not bigger than L_0 / N_L.

The symmetric Cauchy stress tensor $\boldsymbol{\sigma} = \left(\mathbf{t} + \mathbf{t}^T\right)/2$ and the Green strain tensor $\mathbf{E} = \left(\mathbf{F}^T\mathbf{F} - \mathbf{I}\right)/2$ are considered to study the stress/strain concentration behaviors of LCE. The stress concentration factor K_σ and the strain concentration factor K_E are defined as

$$K_\sigma := \max_{X,Y} \sigma_1(X,Y)/\sigma_0 \quad , \quad K_E := \max_{X,Y} E_1(X,Y)/E_0 \tag{30}$$

where $\sigma_1(X,Y)$ and $E_1(X,Y)$ are the first principal stress and principal strain, respectively. σ_0 is the far field value of the stress σ_{xx}, and the strain $E_0 := \left(\lambda^2 - 1\right)/2$.

Fig. 3(b) depicts the mesh dependence of stress/strain concentration factors K_σ and K_E in the sample at three different strains $\varepsilon_0 = \log(\lambda) = 0.05, 10, 20\%$. The mesh dependence of the maxima of the director rotation $|\Delta\theta|_{\max} := \max_{X,Y} |\Delta\theta(X,Y)|$ and the principal spontaneous strain $E^S_{\max} := \max_{X,Y} E^S_1(X,Y)$ are shown in Fig. 3(c). It is

obvious that with N_ρ=24, we have rather good mesh convergence. In this case, the minimal mesh size is $2\ \mu m$ and the total number of elements is about 39000. Thus, we shall use this mesh in the following.

As we have discussed before, when $r=1$ and $a=0$, the semi-soft elastic energy (12) recovers the well-known neo-Hookean model, i.e. $f_{nH}=0.5\mu\mathrm{tr}\left(\mathbf{F}\mathbf{F}^T\right)$. Due to the tight relation between the semi-soft elasticity and the neo-Hookean model, we also made numerical simulations using the neo-Hookean elastic energy as a reference. The sample is stretched quasi statically, and the shear modulus μ, geometric parameters ρ_0 & L_0, and loading conditions of the neo-Hookean model and the LCE model are all the same. Specific comparisons are shown in following sections.

3. Stress and strain concentrations for LCEs in deep nematic phase

We know that all the stress and strain maxima in Fig. 3(b) are attained at the edge of circular hole. Thus, we shall firstly consider their characteristics.

3.1. Stress and strain distributions at the hole edge

It is obvious due to the free boundary condition on the hole edge ($\rho=\rho_0$) that only the tangential component of the Cauchy stress, σ_{tt} can be nonzero. As shown by the left figure in Fig. 4(a) for $\varepsilon_0=0.05\%$, σ_{tt} are tensional (outward arrows) at the upper and lower parts of the circle, and have two equal maxima at the top and the bottom points (A: $\varphi_\sigma^M=\pm 90^\circ$). It becomes compressional (inward arrows) near $\varphi=0^\circ$ and 180°. Although the maximal stress is higher than that of the neo-Hookean (n-H) material, shown by the dashed lines, the stress distribution of the LCE sample is qualitatively similar, which can be better observed in Fig. 4(c). Note that at very small strains, the numerical results of n-H material are identical to the analytical solutions of linear Hooke materials.

However, as shown by the right picture in Fig. 4(a), the distribution of the first principal strain E_1 of the LCE sample is qualitatively different from the n-H and linear Hooke materials. Namely, the locations of the maximal strain do not coincide with the locations of the maximal stress. In fact, we observe 4 strain maxima as indicated by the star signs (B: $\varphi_E^M \neq \varphi_\sigma^M = \pm 90^\circ$) and are also shown in Fig. 4(d); the understanding of the unusual behavior will be provided later in Fig. 6.

Fig. 4(b), (c) and (e) depict the stress and strain distributions on the hole edge at a larger strain $\varepsilon_0 = 10\%$. It is clear that the strain distribution has changed to show only two maxima occurring at the identical locations to those of the maximal stress. Thus, we do always observe larger stress and strain concentrations for a LCE sample than a n-H material, but the qualitatively different strain distributions only occur at relative small loadings, as summarized more clearly in Fig. 5 by using the stress/strain concentration factors, K_σ and K_E.

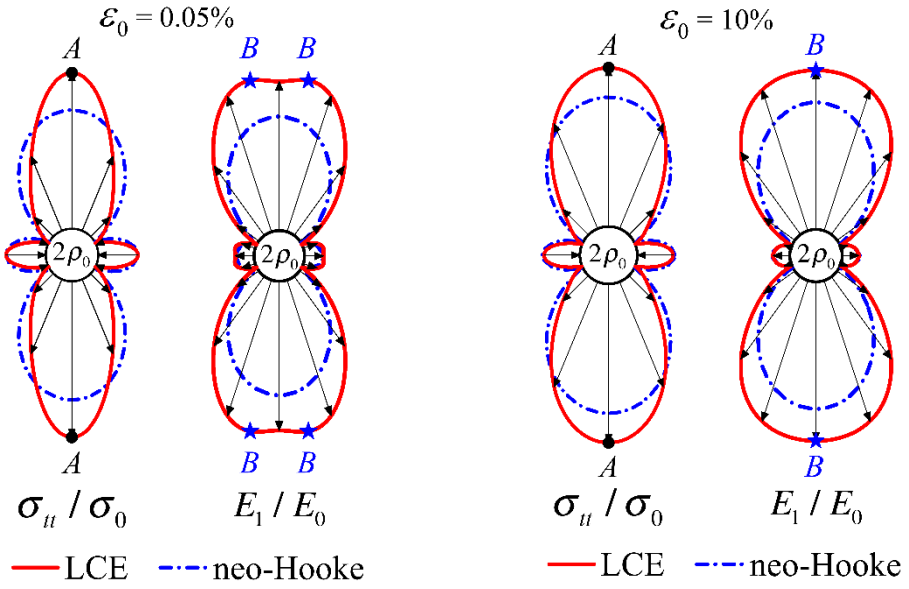

(a) (b)

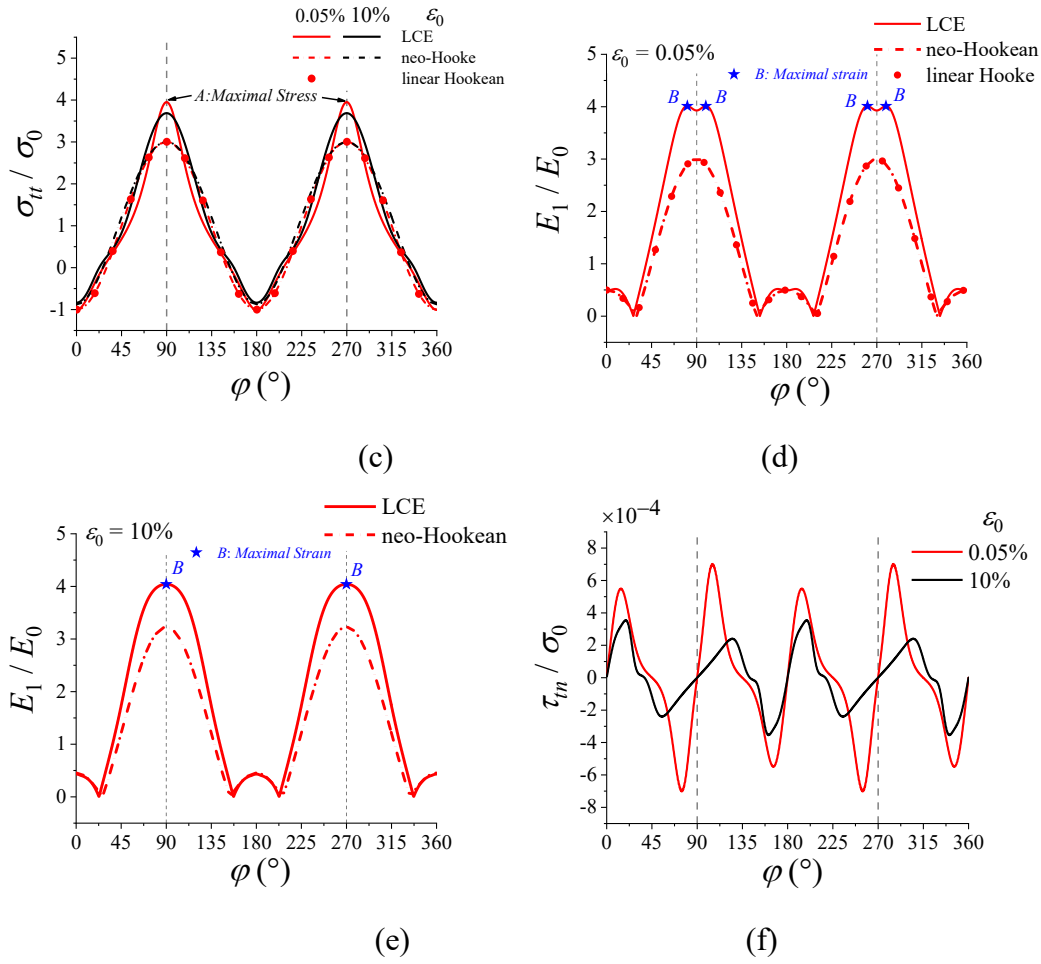

Fig. 4. Distributions of the stress and strain on the hole edge ($\rho = \rho_0$) at small and large strains. The results of a neo-Hookean material and the analytical solutions of a linear Hooke material are plotted for references. (a) and (b) The distributions of the tangential stress σ_{tt} and the principal strain E_1 at $\varepsilon_0 = 0.05\%$ and $\varepsilon_0 = 10\%$, respectively. The outward arrows indicate tensions and the inward arrows indicate compressions. Locations of the maximal stress and strain are labeled as A with a dot and B with a star, respectively. (c) σ_{tt} vs. φ at $\varepsilon_0 = 0.05\%$ and $\varepsilon_0 = 10\%$. (d) and (e) E_1 vs. φ at $\varepsilon_0 = 0.05\%$ and $\varepsilon_0 = 10\%$, respectively. (f) The skew-symmetric stress τ_{tn} vs. φ at $\varepsilon_0 = 0.05\%$ and $\varepsilon_0 = 10\%$. All stresses and strains are scaled with the corresponding far field value σ_0 and strain E_0. Compared to a neo-Hookean sample, a LCE sample shows higher concentrations of both the stress and the strain with four concentration locations of the strain at a small prescribed strain, $\varepsilon_0 = 0.05\%$.

The elastic stress and strain field of finite thickness plate containing a hole under uniaxial tension are numerically investigated, and non-coincidence of the locations of the stress and strain concentrations was found (Yang, 2009; Yang et al., 2008). The concentration locations at the circular hole are generally not on the mid-plane and can be different for the stress and the strain. However, no similar results for plane problems are known to us. Thus, the strain concentration behavior of LCE seems very unusual.

Moreover, we can observe from Fig. 5(a) that K_E of LCE is not only much larger than that of n-H materials but also its strain dependence is qualitatively different. Namely, $K_E(\varepsilon_0)$ of LCEs decreases slightly and reaches a minimum at a loading ε_0^m before increases with the loading, while $K_E(\varepsilon_0)$ of n-H materials increases monotonically with the loading.

The Cauchy stress concentration factor $K_\sigma(\varepsilon_0)$ of LCE is always larger than that of n-H materials. The $K_\sigma(\varepsilon_0)$ can decrease slightly before increasing with the deformation. A similar non-monotonic $K_\sigma(\varepsilon_0)$ was reported for uniaxially stretched rubber sheets with a circular hole (Khajehsaeid et al., 2016). They have attributed that to possibe load induced geometric nonlienarities.

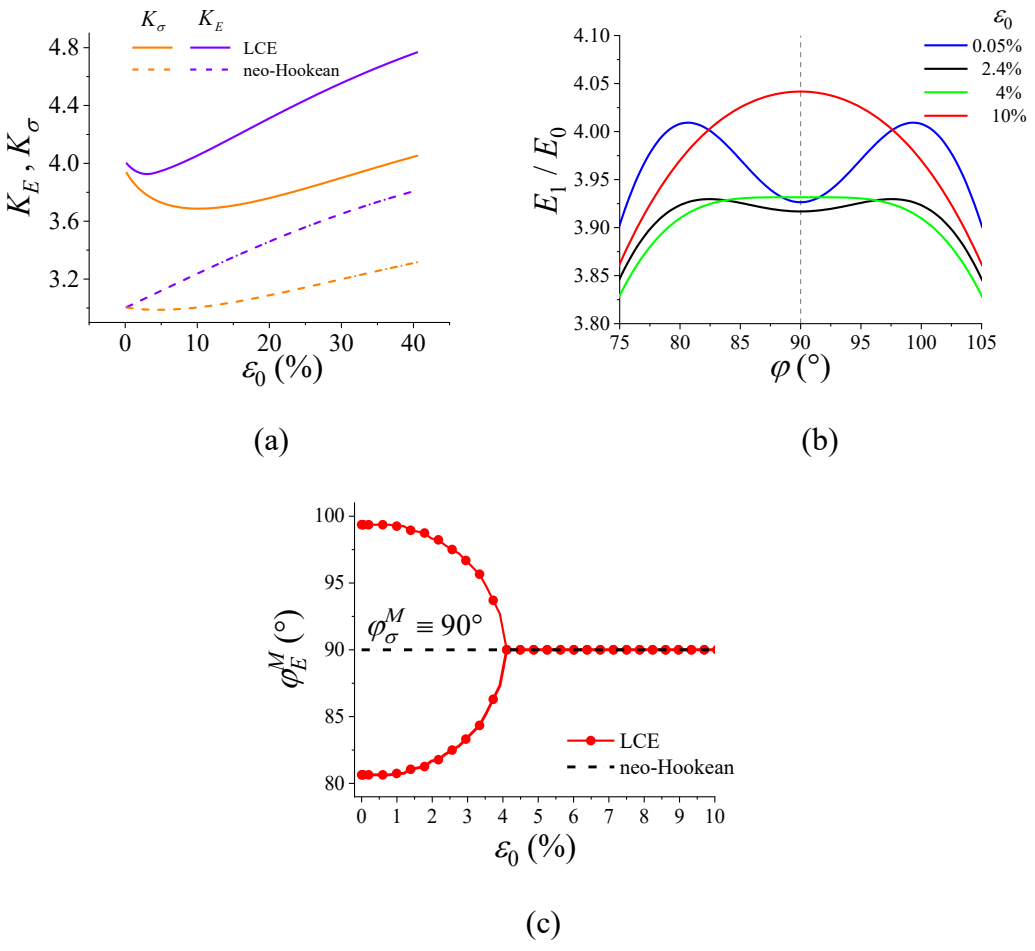

Fig. 5. Strain dependences of the factors and the locations of the stress/strain concentrations of LCEs in comparison with the neo-Hookean material. (a) Dependence of the stress/strain

concentration factors of the symmetric Cauchy stress K_σ and the Green strain tensor K_E on the prescribed strain ε_0. (b) Distributions of the principal strain E_1 near the location of stress concentration ($\varphi_\sigma^M = 90°$) at different prescribed strain ε_0; (c) Dependence of the locations of the strain concentrations on the prescribed strain ε_0.

As shown in Fig.4(f), we have nonzero skew-symmetric part of the stress tensor, τ_{tn} at the hole edge. Its maximal value is much smaller (at least three magnitudes smaller) than the symmetric part σ_{tt} shown in Fig. 4(c). Thus, it should have little effect on the stress equilibrium equation (24). Nevertheless, it is the driving force for the stress induced director rotation governed by (26) as we shall consider next.

3.2 Director rotations and spontaneous strains on the hole edge

It is known that for prolate LCEs under tensile loading, the director $\mathbf{d}$ will rotate towards the loading axis. Thus, for our sample as in Fig. 2(a) with the initial director $\mathbf{d}_0$ parallel to the loading axis, no director rotations can occur, i.e. $\mathbf{d} = \mathbf{d}_0$ at positions far away from the hole. However, on the stress free hole edge, the stress distribution is very different from the uniaxial state. In fact, the only nonzero stress component is the tangential one, σ_{tt} as shown in Fig. 4(a) and (b). Hence, we would expect that the director will rotate to the tangential direction when $\sigma_{tt} > 0$, but to the normal direction when $\sigma_{tt} < 0$. Moreover, the director is expected to rotate more when the stress is higher. Fig. 6(a) and (b) have confirmed these properties. At the location of the maximal stress, $\varphi_\sigma^M = 90^\circ$, there is no director rotation ($\Delta\theta(90^\circ) = 0$), because the initial director $\mathbf{d}_0$ is already in the tangential direction ($\theta_0 = 0$). In the region $0° < \varphi < 90^\circ$, the directors rotate clockwise ($\Delta\theta < 0$) when $\sigma_{tt} > 0$ but anticlockwise ($\Delta\theta > 0$) when $\sigma_{tt} < 0$. There is no rotation at $\varphi = 0^\circ$ with $\sigma_{tt} < 0$, because $\mathbf{d}_0$ is already in the normal direction.

The rotation of the directors in LCEs will result in the spontaneous strains $\mathbf{B}^S$ in (19) that affects the bulk stress $\boldsymbol{\sigma}^{bulk}$ in (18). To represent the spontaneous strains in

the Lagrange coordinate, we can rewrite the stress-strain relation (18) as

$$\boldsymbol{\sigma}^{bulk} = -p\mathbf{I} + 2\mu\mathbf{R}\left(\mathbf{E} - \mathbf{E}^{S}\right)\mathbf{R}^{T} \tag{31}$$

where $\mathbf{R}$ is the rigid body rotation in the polar decomposition of the deformation gradient ($\mathbf{F} = \mathbf{RU}$) and $2\mathbf{E} = \mathbf{U}^2 - \mathbf{I}$ is the Green strain. Then, by (19) we can obtain the spontaneous strain, $\mathbf{E}^{s}$ in the reference configuration as

$$\mathbf{E}^{S} := \frac{1}{2}\mathbf{R}^{T}\mathbf{B}^{S}\mathbf{R} = \frac{1}{4}\left(\mathbf{R}^{T}\mathbf{d}\otimes\mathbf{R}^{T}\hat{\mathbf{g}}^{b} + \mathbf{R}^{T}\hat{\mathbf{g}}^{b}\otimes\mathbf{R}^{T}\mathbf{d}\right) - \frac{r-1}{2}\mathbf{U}\mathbf{d}_{0}\otimes\mathbf{U}\mathbf{d}_{0} \tag{32}$$

Fig. 6(b)-(d) depict the distributions of the principal spontaneous strain E_1^s and the three components, $E_{\rho\rho}^s$, $E_{\varphi\varphi}^s$ and $E_{\rho\varphi}^s$, which are all rather big and are comparable with the applied strain, $E_0 = (\lambda^2 - 1)/2$. Their contributions to the total strains are quite obvious in Fig. 6(e) and (f). While for n-H materials the shear component, $E_{\rho\varphi}$, is identically zero on the stress free edge, for LCEs $E_{\rho\varphi}$=$E_{\rho\varphi}^s$ vanishes only at $\varphi = 0^\circ, \pm 90^\circ, 180^\circ$, where there is no director rotation, i.e. $\theta = \theta_0 = 0$.

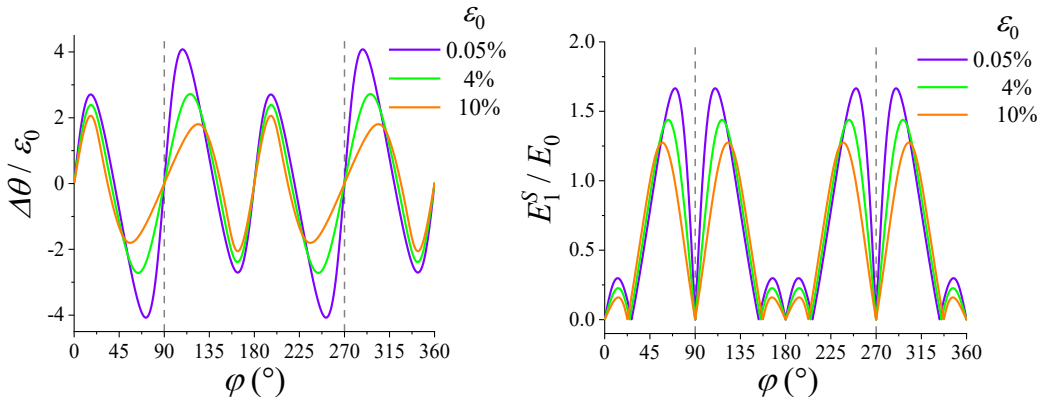

(a) (b)

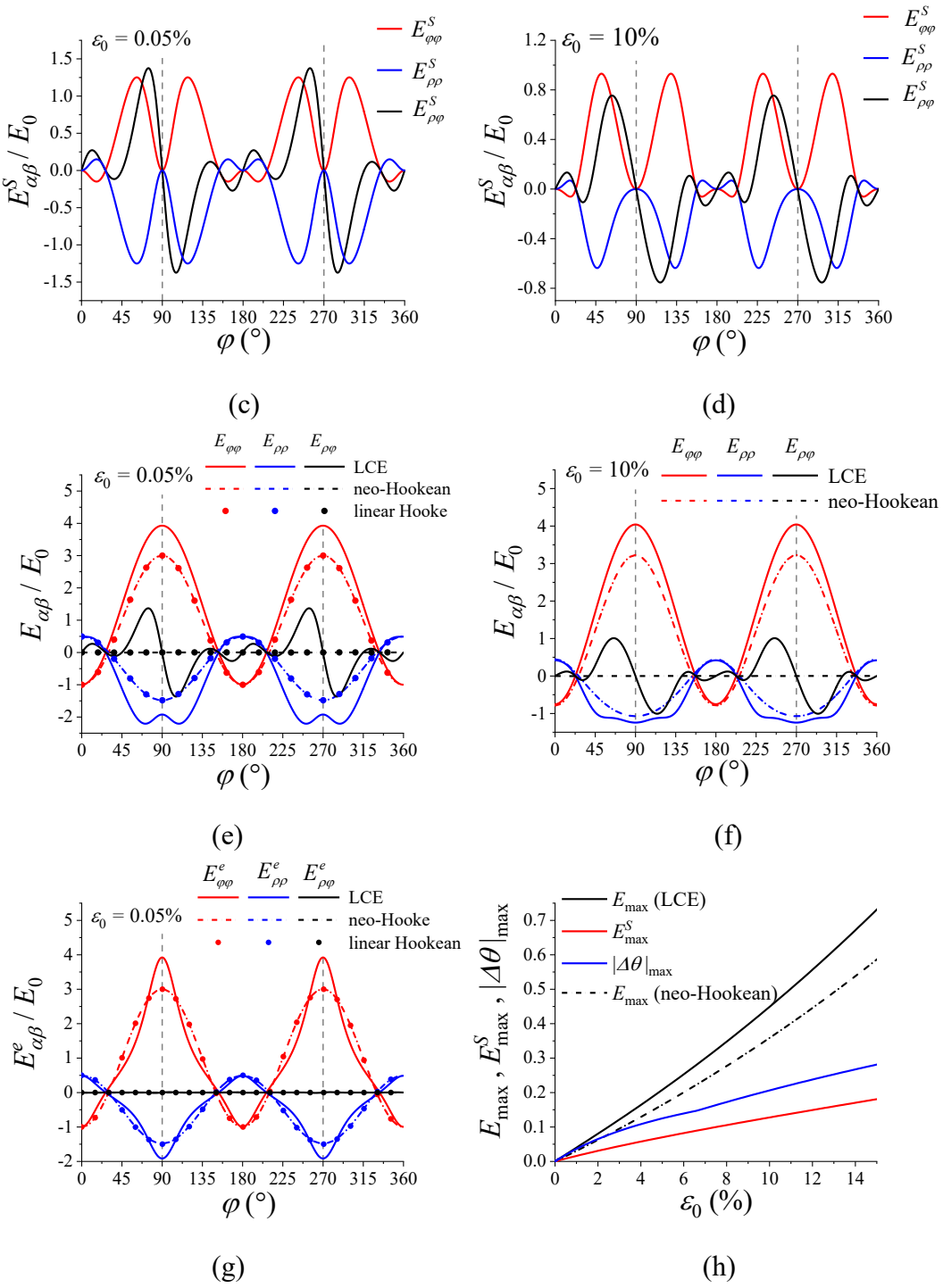

Fig. 6. The distributions of the director rotation, and the spontaneous, the elastic and the total strains on the hole edge at prescribed strains, in comparison with those of the neo-Hookean materials and the analytical solutions of linear Hooke material. Distributions on the hole edge of (a) the director rotation $\Delta\theta$ (in radians); (b) the principal spontaneous strain E_1^S; (c) and (d) the spontaneous strain components $E^s_{\rho\rho}$, $E^s_{\varphi\varphi}$ and $E^s_{\rho\varphi}$; (e) and (f) the total strain components $E_{\rho\rho}$, $E_{\varphi\varphi}$ and $E_{\rho\varphi}$; (g) the elastic strain components $E^e_{\rho\rho}$, $E^e_{\varphi\varphi}$ and $E^e_{\rho\varphi}$;. (h) Loading dependence of the maxima of the director rotation $|\Delta\theta|_{\max}$ (in radians), the first principal spontaneous strains

$E^s_{\max}$ and the first principal strain $E_{\max}$. The spontaneous strains resulted from the director rotations on the hole edge have made the total strains of a LCE sample very different from a neo-Hookean material, and is the main cause for the unusual concentration behavior of a LCE.

To understand the distributions of the other two components, $E_{\rho\rho,\varphi\varphi}$, let us first consider the small loading case, $\varepsilon_0 \ll 1$. Then, the Green strain $\mathbf{E}$ is reduced to the Cauchy strain, $\boldsymbol{\varepsilon} := \left(\nabla\mathbf{u} + \nabla\mathbf{u}^T\right)/2$, and can be decomposed into the elastic and spontaneous part as, $\boldsymbol{\varepsilon} = \boldsymbol{\varepsilon}^e + \boldsymbol{\varepsilon}^s$. The spontaneous strain $\boldsymbol{\varepsilon}^s = \mathbf{E}^s$ is shown in Fig. 6(c). The elastic strain $\boldsymbol{\varepsilon}^e$ can be calculated from the stress $\boldsymbol{\sigma}$ by using the isotropic incompressible linear Hooke's law as $\varepsilon^e_{\varphi\varphi} = \left(\sigma_{\varphi\varphi} - 0.5\sigma_{\rho\rho}\right)/3\mu$ and $\varepsilon^e_{\rho\rho} = \left(\sigma_{\rho\rho} - 0.5\sigma_{\varphi\varphi}\right)/3\mu$. It is obvious by Fig. 6(g) that the elastic strains of LCEs is qualitatively the same as n-H. Namely, the elastic shear $\varepsilon^e_{\varphi\rho} = \sigma_{\varphi\rho}/2\mu$ vanishes at the free edge and the other two components $\varepsilon^e_{\varphi\varphi,\rho\rho}$ reach the extrema at the locations of the stress concentrations, $\varphi^M_\sigma = \pm 90^\circ$. Thus, the unusual deviation of the locations of the strain concentration φ^M_E from $\varphi^M_\sigma = \pm 90^\circ$ at relative a small loading as shown in Fig. 4(a) and (c) and Fig. 5(b) and (c) should be resulted from the contribution of the spontaneous part $\boldsymbol{\varepsilon}^s = \mathbf{E}^s$.

At larger loadings, the qualitative characteristics of the director rotations (Fig. 6(a)), and the elastic and spontaneous strains (Fig. 6(b)-(f)) does not change, but the relative contributions of the spontaneous part become smaller as indicated more clearly in Fig. 6(h). Namely, although the maxima, $\left|\Delta\theta\right|_{\max}$, $E^s_{\max}$, and $E_{\max}$ all increase with the loading, the first two curves show slight decreasing slopes while the total strain raises with a growing slope. Hence, at large loadings, the elastic strain becomes more dominant and the locations of the strain concertation will move to coincide with those of the stress as shown by Fig. 5(b) and (c).

To understand the reason why the director rotations near the hole edge lead to stronger stress and strain concentrations of LCEs, we will next analyze the behavior of the whole sample.

3.3 Director rotations and the energy reductions

As the director is initially aligned to the loading axis, $\theta_0 = 0$, stress induced director rotations only occurs near the free edge of hole as shown in Fig. 7(a) and (b). In the region far away from the hole, ca. $\rho / \rho_0 \geq 15$, there are no director rotations and the stress state becomes uniaxial, same as in regular elastic materials, i.e. $\sigma_{xx} = \sigma_0$, $\sigma_{yy} = \sigma_{xy} = 0$, as shown clearly in Fig. 7(c), (d) and (e). For an infinite large sheet, the far-field stress and the free energy of a LCE sample should be equal to the n-H sample with the same modulus. Nevertheless, we do observe an interesting phenomenon that the stress σ_{xx} of the LCE sample within an intermediate region can be slightly smaller than the n-H material, as shown more clearly in Fig. 7(h) by using the relative difference.

To understand the phenomenon systematically, we consider the energy $F(\rho_A)$ by integrating the free energy density f of (9) within the region $\rho_0 \leq \rho \leq \rho_A$ at the initial configuration, $F(\rho_A) = \int_{\rho_0}^{\rho_A} \int_0^{2\pi} f d\varphi d\rho$. The energy $F_{IR} := F(50\rho_0)$ is calculated to represent the energy within the intermediate region around the hole edge. Obviously, it increases with the loading, as shown in Fig. 7(f), but is always a little bit smaller than the corresponding n-H sample as shown more clearly in Fig. 7(h) by using their relative difference. For comparison, $F_{HE} := F(1.1\rho_0)$ is calculated to represent the energy concentrated nearby the hole edge. We find that F_{HE} also increases with the loading but is always bigger than the n-H material, as shown in Fig. 7(g) and (h). Moreover, by (9) and (12), the total free energy of LCEs has three contributions, the soft F^s (by integrating f_s), the semi-soft F^{ss} (by f_{ss}) and the Frank energy F^{Frank} (by f_{Frank}) as shown in Fig. 7(f) and (g). Physically speaking, the soft elastic energy, F^s, also named the Trace formula or neo-classical model (Warner and Terentjev, 2007), reflects the elasticity of the polymer backbone and it increases with the loading in the intermediate region and on the hole edge. The semi-soft elastic energy, F^{ss}, is due to the constraint of the backbone on the director rotations. The director rotation, and therefore F^{ss}, increases with the loading, but is limited in the region near the hole edge. Namely, F^{ss} contributes more than 5% to the total energy and increases with the loading on the hole edge in Fig. 7(g), but is very small in the intermediate region as in Fig. 7(f). On the other hand, due to the very small Frank constant in (28),

$F_{IR,HE}^{Frank}$ is always negligibly small (5~6 magnitudes smaller than $F_{IR,HE}^{ss}$).

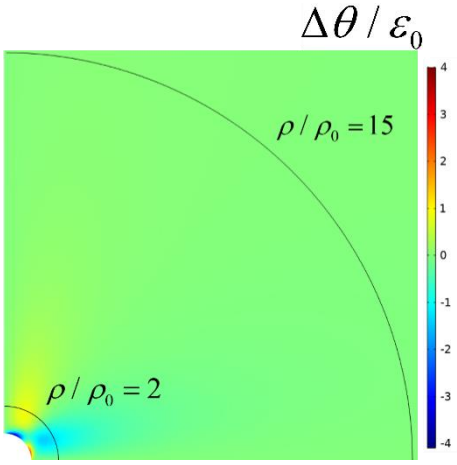

(a)

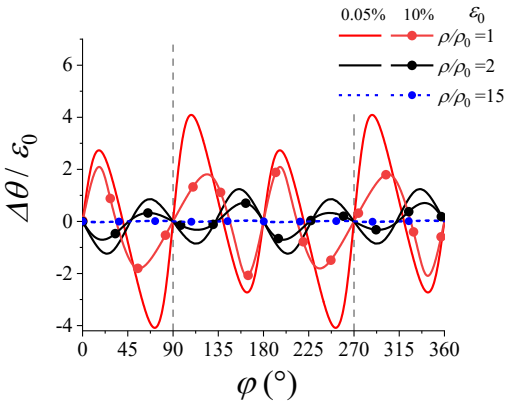

(b)

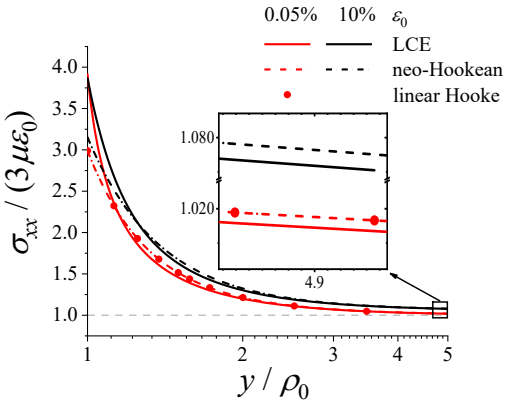

(c)

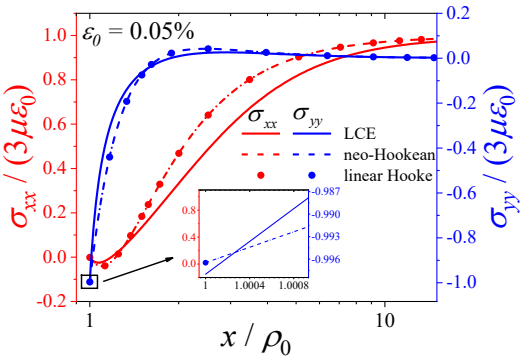

(d)

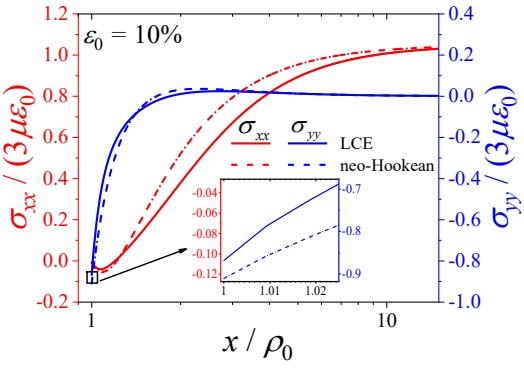

(e)

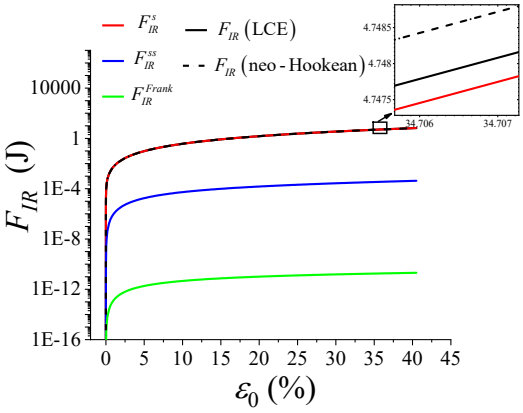

(f)

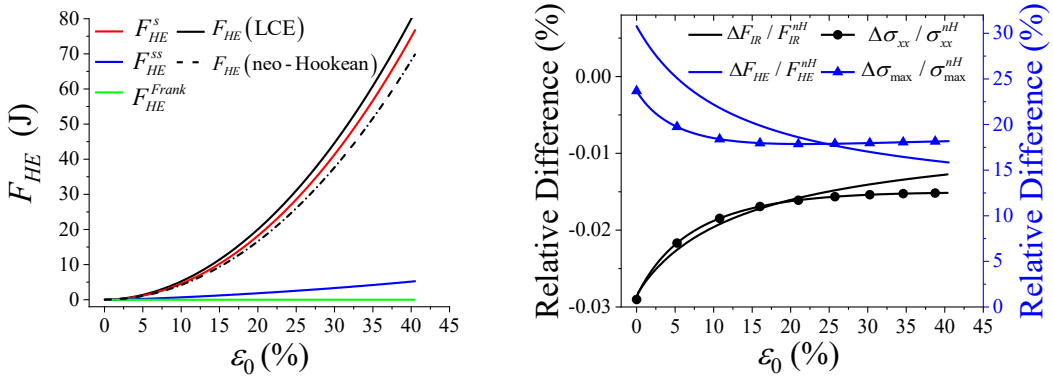

(g) (h)

Fig. 7. Distributions of the director rotations and stresses in the sample and variation of the free energies of LCEs in comparison with a neo-Hookean material and the analytical solutions of a linear Hooke material. (a) The contour plot of $\Delta\theta$ at $\varepsilon_0 = 0.05\%$. (b) Distributions of $\Delta\theta$ along the paths $\rho/\rho_0 = 1,\ 2,\ 15$ marked in (a). (c) Dependence of σ_{xx} on y at $x = 0$, i.e. $\varphi = 90°$. (d) and (e) Dependence of σ_{xx} and σ_{yy} on x at $y = 0$, i.e. $\varphi = 0°$ at strain $\varepsilon_0 = 0.05\%$ (d) and $\varepsilon_0 = 0.05\%$ (e). (f) The representative free energy in the intermediate region $F(50\rho_0)$ vs. ε_0. The three energy terms, the soft energy F^s, semi-soft energy F^{ss} and the Frank energy F^{Frank} are also plotted. (g) The representative energies on the hole edge $F(1.1\rho_0)$ vs. ε_0. (h) The relative differences of σ_{xx} at $\rho/\rho_0 = 50$, $\sigma_{\max} := \max_{X,Y} \sigma_1(X,Y)$, F_{IR} and F_{HE} between the samples of LCE and the neo-Hookean material. ($\Delta F := F^{LCE} - F^{nH}$, $\Delta\sigma_{xx} := \sigma_{xx}^{LCE} - \sigma_{xx}^{nH}$, $\Delta\sigma_{\max} := \sigma_{\max}^{LCE} - \sigma_{\max}^{nH}$) Under a prescribed strain, the director rotations and the resulting stronger stress/strain concentrations around the hole leads to lower stresses and smaller total free energy in the intermediate region of a LCE comparing to a neo-Hookean material.

For a flawless sample subjected to uniaxial tension, if the initial director $\mathbf{d}_0$ is parallel to the loading axis, the far-field stress and total free energy of the LCE sample are equal to those of a neo-Hookean material, which can be easily proved by inserting $\mathbf{d} = \mathbf{d}_0$ into (14). However, the behaviors of samples containing a hole seem to be different. We can observe that there are relatively large director rotations near the free hole edge of a LCE sample. The localized director rotations result in stronger stress and strain concentrations on the hole edge, and make the stress and free energy within an intermediate region lower than those of n-H materials at the same prescribed strain. Large spontaneous strains are induced by the director rotations, and their contributions to the total strain can make the concentration locations of strain different from those of stress.

Inspired by the fascinating programmability of LCEs, we may be able to reduce the stress/strain concentrations and therefore prevent potential failures by designing the local director distribution around the hole edge. According to our primary attempts, it seems that the stress concentration is relieved by setting the angle between the initial director of an arbitrary point on the hole edge and its tangential direction as a constant. The director within the high-stress region, in this way, might rotate in the same direction and have a softening effect on the stress. The designing will be studied specially in some future works.

4. Effects of the backbone anisotropy and semi-softness

As we know from the previous experimental and theoretical studies (Warner and Terentjev, 2007; Zhang et al., 2020), the soft-elastic behavior of LCEs should depend strongly on the material properties, especially the step length ratio r ($r>1$ for prolate LCEs) and the semi-soft coefficient $a>0$. A smaller a implies a weaker constraint of the backbone network on the director rotation, so bigger director rotations would be expected near the hole edge under the same loading. A larger r means stronger anisotropy of the backbone molecules, so larger spontaneous strains can be induced. We shall consider their effects on the stress and strain concentrations in this section.

As discussed extensively by Warner and Terentjev (Warner and Terentjev, 2007), the two material parameters, r and a, can be quite different for LCE samples with different polymer systems and preparation methods. For a given sample, they can vary strongly with the testing temperature as well. In the following, we shall consider two types of monodomain side-chain nematic elastomers that have been widely studied, the polysiloxane LCEs and the polyacrylate LCEs.

As we have discussed in Sect. 2.5, the exact values of two viscous constants η_b and η_d in (28) are not so important for our numerical calculations as long as the

conditions $\dot{\lambda}t_b \ll 1$ and $\dot{\lambda}t_d \ll 1$ are satisfied by (29). Thus, we consider only the effect of the step length ratio r and the semi-soft coefficient a, and keep all other parameters as in (28) and (29). In addition, we have checked the convergence of all the samples in Sect. 4 as we do in Fig. 3.

4.1 Stress/strain concentration behavior of polysiloxane LCEs

Table 1 listed the values of the backbone anisotropy r and the semi-soft coefficient a reported (Finkelmann et al., 1997) for polysiloxane side-chain LCE monodomain samples prepared by using the two-step crosslink process with different crosslink densities. It is obvious that the larger the crosslink density, the larger the semi-soft coefficient a as it represents the constraint of the backbone networks as indicated by (14). Fig. 8(a) and (b) depict that both the stress and the strain concentration factors $K_\sigma(\varepsilon_0)$ and $K_E(\varepsilon_0)$ become smaller for stronger crosslinks. For the sample with the densest crosslinks (15%), we observe a monotonically increasing $K_E(\varepsilon_0)$ similar to that of a neo-Hookean material. All the other behaviors are qualitatively similar to the deep nematic example (DNE) studied in the previous section.

Table 1. Material parameters used in Fig. 8 – Fig. 10 and the coupling constant $D_2 := r - 1/r + a$. The parameters r and a of both polysiloxane and poyacrylate side-chain LCEs *are obtained from the referenced experimental results.* For polysiloxane LCEs using the two-step crosslink method, the parameters for samples with different crosslinking densities (Finkelmann et al., 1997) and different testing temperatures (Petelin and Copic, 2010) are listed. Table. 1 also lists the parameters of polyacrylate LCEs with different alignment methods: the magnetic field by R1997 (Roberts et al., 1997), the mechanical stretch by Z1999 (Zubarev et al., 1999), the one-step photo-polymerization by H2013 (Higaki et al., 2013). The parameters of the sample studied in Section 3 are also listed as the Deep Nematic Elastomer (DNE).

	Polysiloxane side-chain LCEs						Polyacrylate side-chain LCEs			Deep Nematic Elastomer (DNE)
	Finkelmann et al 1997			Copic and Petlin 2010			R1997	Z1999	H2013	
	10%	12.5%	15%	60℃	70℃	75℃				
r	2.6	2.6	2.6	2.6	1.95	1.28	1.29	1.44	2.1	1.8

a	0.113	0.153	0.2211	0.11	0.094	0.042	0.05	0.03	0.14	0.1
D_2	2.3284	2.3684	2.4365	2.3254	1.5312	0.5408	0.5648	0.7756	1.7638	1.3444

All the concentration locations of the strain $\varphi_E^M(\varepsilon_0)$ do not coincide with those of the stress, $\varphi_\sigma^M = \pm 90^\circ$, at relatively small loadings, as shown in Fig. 8(c). However, we observe that in the two samples with high crosslink densities 10% and 12.5%, the location differences of the strain and stress concentrations $\left|\varphi_E^M - \varphi_\sigma^M\right|$ can slightly increase with strain before decreasing at larger loadings.

Relatively large director rotations and spontaneous strains are induced around the hole edge in the polysiloxane LCEs similar to those in Fig. 6 and 7 for the DNE. Their maxima, as shown in Fig. 8(d) and (e), increase with the loading, and are smaller for samples with denser crosslinks. Thus, we do observe a correlation between the stress/strain concentration behavior and the spontaneous strains resulted from the director rotations.

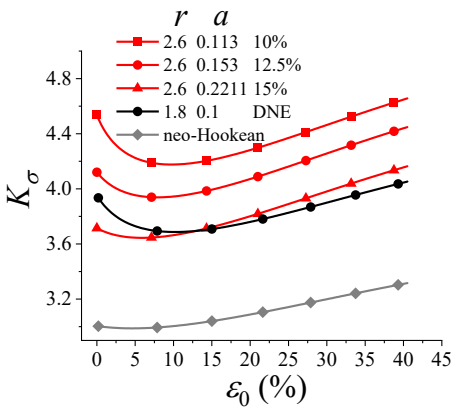

(a)

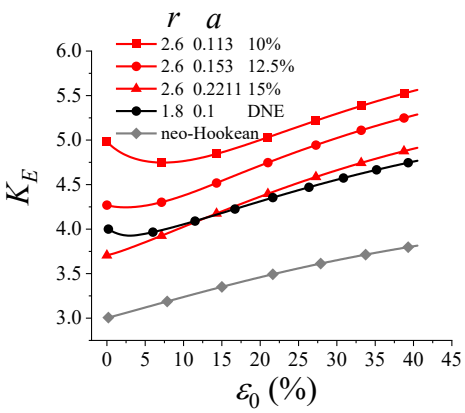

(b)

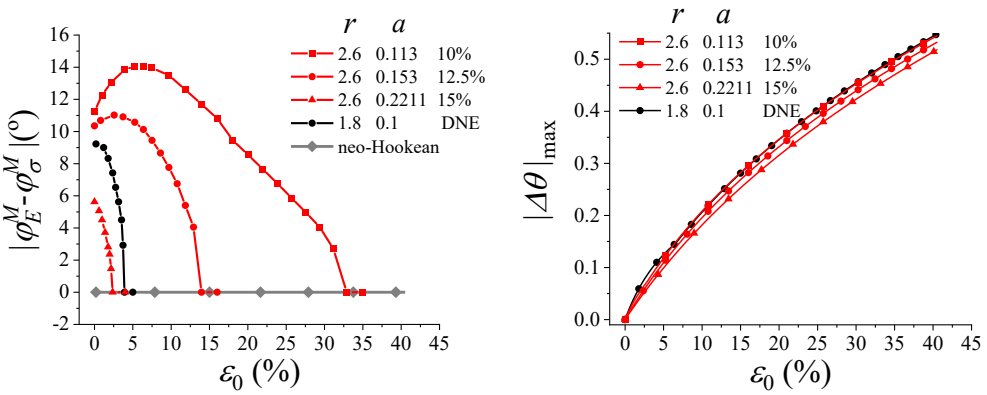

(c)

(d)

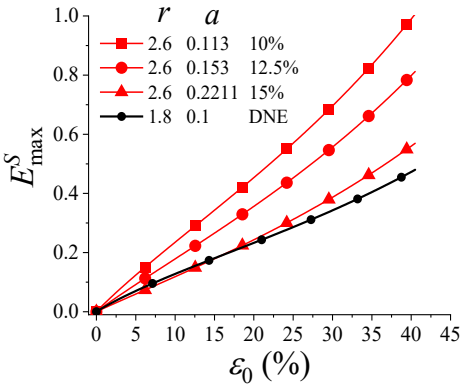

(e)

Fig. 8. Effect of crosslink density on the stress/strain concentration behaviors for monodomain samples of polysiloxane side-chain nematic elastomers using the two step crosslink method (Finkelmann et al. 1997) with the parameters listed in Table 1. The neo-Hookean and the deep nematic example (DNE) studied in the previous section are plotted for comparison. (a) Stress concentration factors K_σ vs. ε_0. (b) Strain concentration factor K_E vs. ε_0. (c) Differences of the concentration locations of strain and stress $\left|\varphi_E^M-\varphi_\sigma^M\right|$ vs. ε_0. (d) The maximal director rotation $|\Delta\theta|_{max}$ vs. ε_0. (e) The maximal spontaneous strain E^S_{max} vs. ε_0. As the crosslink density decreases, the director rotation and the spontaneous strain increase, resulting in stronger the stress/strain concentrations.

For a given polysiloxane LCE sample, we know that both r and a can decrease significantly with the testing temperature as they are closely related to the order parameter of the liquid crystal phase. Table 1 also lists the values r and a at different experimental temperatures (Petelin and Copic, 2010). As the testing temperature increases from 60 to 75 °C, r is reduced by half and a is reduced to

nearly one-third. As a result, both $K_\sigma(\varepsilon_0)$ and $K_E(\varepsilon_0)$ become much smaller, as shown in Fig. 9(a) and (b).

Fig. 9(c) depicts that the concentration locations of the strain, $\varphi_E^M(\varepsilon_0)$ at $T=60°C$ and $70°C$ are similar to those in the previous cases, i.e. $\left|\varphi_E^M-\varphi_\sigma^M\right|$ is nonzero and slightly increases at small ε_0. However, we observe $\varphi_E^M\equiv\varphi_\sigma^M=\pm90°$ at $T=75°C$, which is very close to the nematic-isotropic transition point. Fig. 9(d) and (e) depict that at a higher temperature the maximal director rotation is slightly larger but the resulting spontaneous strain is smaller. Thus, similar to the previous observation, a larger the spontaneous strain leads to stronger the stress/strain concentrations and far positions φ_E^M away from $\varphi_\sigma^M=\pm90°$. However, there seems no direct correlation between the director rotations in Fig. 9(d) and the spontaneous strains in Fig. 9(e). More discussions will be given in Sect. 4.3.

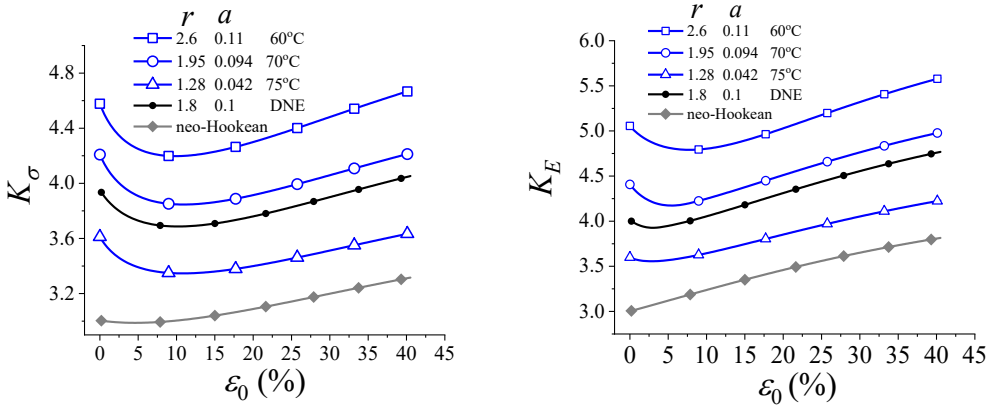

(a)

(b)

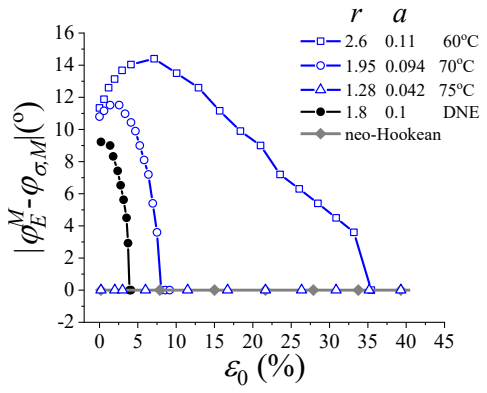

(c)

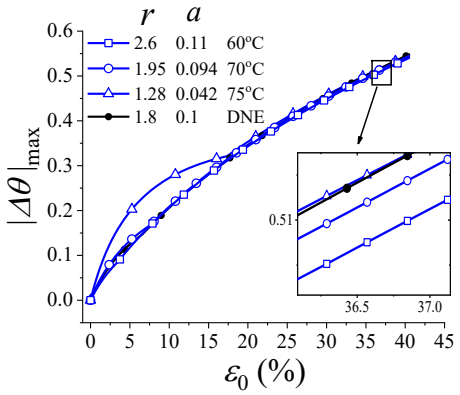

(d)

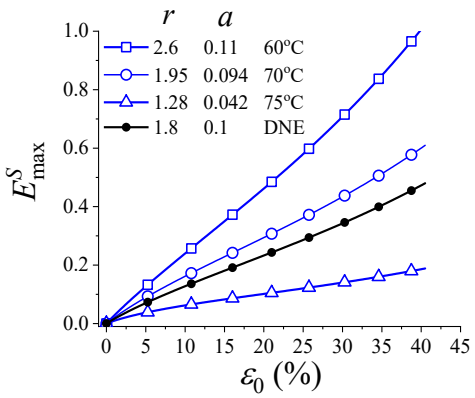

(e)

Fig. 9. Effect of the testing temperature on the stress/strain concentration behaviors for monodomain samples of polysiloxane side-chain nematic elastomers (Petelin and Copic, 2010) with the parameters listed in Table 1. The neo-Hookean and the deep nematic example (DNE) studied in the previous section are plotted for comparison. (a) Stress concentration factors K_σ vs. ε_0. (b) Strain concentration factor K_E vs. ε_0. (c) Differences of the concentration locations of strain and stress $\left|\varphi_E^M - \varphi_\sigma^M\right|$ vs. ε_0. (d) The maximal director rotation $|\Delta\theta|_{\max}$ vs. ε_0. (e) The maximal spontaneous strain $E^S_{\max}$ vs. ε_0 .As the testing temperature increases, the spontaneous strain and the stress/strain concentrations decrease. No clear temperature dependence of the director rotation is observed.

4.2 Stress/strain concentration behavior of polyacrylate LCEs

It is known that both r and a are generally smaller for monodomain samples made of polyacrylate side-chain nematic elastomers than the polysiloxane LCE considered above. And they can be quite different for samples prepared with different methods as summarized in Table 1. Nevertheless, Fig. 10(a) and (b) show that both $K_\sigma(\varepsilon_0)$ and $K_E(\varepsilon_0)$ are always larger than those of a neo-Hookean material and have the same non-monotonic ε_0 dependence, i.e. the stress concentration factors decrease and increase as ε_0 increases. $K_\sigma(\varepsilon_0)$ and $K_E(\varepsilon_0)$ for the sample Z1999 prepared by the two-step crosslink method (Zubarev et al., 1999) are the biggest at small strains, but those for the sample H2013 prepared by the one step photo-polymerization (Higaki et al., 2013) become the highest at larger loadings. Such crossover of $K_\sigma(\varepsilon_0)$

and $K_E(\varepsilon_0)$ at some large ε_0 have also been observed in Fig. 8(a) and (b) between DNE and the sample with 15% crosslink density.

While the locations for the stress concentration are always at $\varphi_\sigma^M = \pm 90^\circ$, the locations for the maximal strains, φ_E^M, are quite different for the three samples as shown by Fig. 10(c). While $\left|\varphi_E^M - \varphi_\sigma^M\right|$ for the sample Z1999 is nonzero and non-monotonic with respect to ε_0, it is monotonic for the sample H2013, and always zero for the sample R1997, which was prepared by using the magnetic field to align the director (Roberts et al., 1997).

Fig. 10(d) depicts clearly that the maximal director rotation $\left|\Delta\theta\right|_{\max}(\varepsilon_0)$ is always bigger for samples with a smaller semi-soft coefficient a. However, its effect on the maximal spontaneous strains $E^S_{\max}(\varepsilon_0)$ is more complex as shown in Fig. 10(e). $E^S_{\max}(\varepsilon_0)$ of Z1999 is highest at small strains but becomes smaller than H2013 for larger loadings, while $E^S_{\max}(\varepsilon_0)$ of R1997 is always rather small. Crossovers of $\left|\Delta\theta\right|_{\max}(\varepsilon_0)$ and $E^S_{\max}(\varepsilon_0)$ between polysiloxane or polyacrylate LCEs and DNE occur in Fig. 8(d-e), Fig. 9(d) and Fig. 10(d-e).

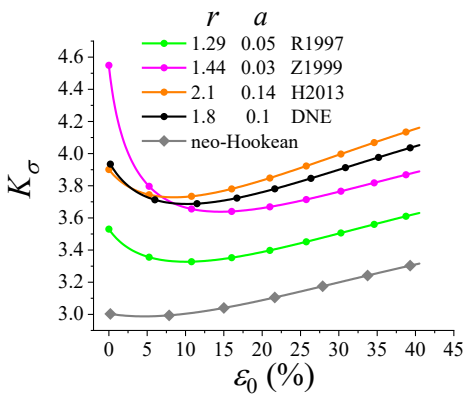

(a)

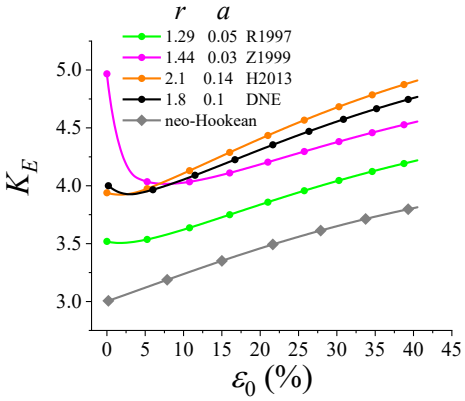

(b)

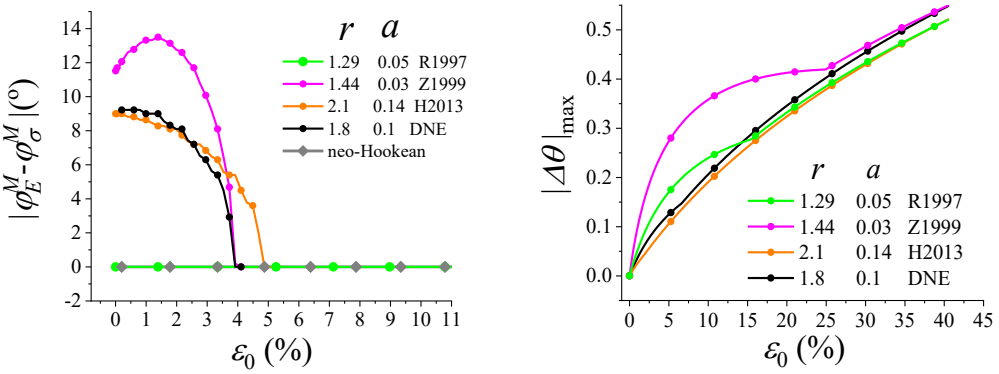

(c)

(d)

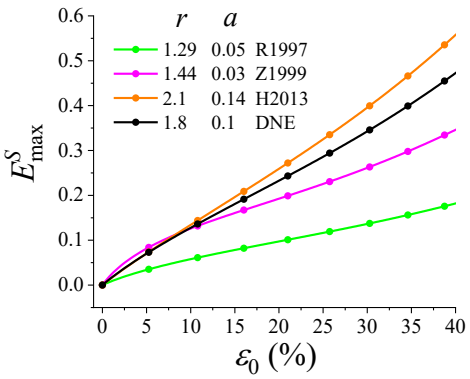

(e)

Fig. 10. Effect of preparation methods on the stress/strain concentration behaviors for monodomain samples of polyacrylate side-chain nematic elastomers with the parameters listed in Table 1. R1997, Z1999 and H2013 are the samples from Roberts at al. 1997, Zubarev et al. 1999 and Higaki et al 2013, respectively. The neo-Hookean and the deep nematic example (DNE) studied in the previous section are plotted for comparison. (a) Stress concentration factors K_σ vs. ε_0. (b) Strain concentration factor K_E vs. ε_0. (c) Differences of the concentration locations of strain and stress $\left|\varphi_E^M - \varphi_\sigma^M\right|$ vs. ε_0. (d) The maximal director rotation $|\Delta\theta|_{max}$ vs. ε_0. (e) The maximal spontaneous strain E_{max}^S vs. ε_0.

4.3 The net director rotation and the parameter dependence

The above studies have demonstrated clearly that the stress and strain concentration factors $K_\sigma(\varepsilon_0)$ and $K_E(\varepsilon_0)$ of LCE thin sheets with a small circular hole are always bigger than those of n-H materials. This can be attributed to the director

rotation around the edge of the circular hole and its effect on the stress distributions. However, the strain dependences of $K_\sigma(\varepsilon_0)$ and $K_E(\varepsilon_0)$ seem quite different for different samples. To quantify the effect of the material parameters on the concentration behavior, we will recall the results in Sect. 3.2 and 3.3, and first analyze the director rotation.

By (25) and (26), we observe that the skew-symmetric Leslie stress and the left hand side of the evolution equation for the director rotation are proportional to $\dot{\theta} - W_{yx}$ with W_{yx} representing the rate of rigid body rotations. Thus, we should consider the net director rotation, $\Delta_{net}\theta := \Delta\theta - \omega_{yx}$ with $\omega_{yx} := \left(v_{,x} - u_{,y}\right)/2$ the skew-symmetric component of the displacement. As shown in Fig. 11(a) and (b), the distributions of $\Delta_{net}\theta$ around the edge of the circular hole are similar to but different from $\Delta\theta$ since the rigid body rotation ω_{yx} does have some contributions, especially at relatively large strains, e.g. at $\varepsilon_0 = 40\%$ in Fig. 11(b). More interestingly, as shown in Fig. 11(c), $\left|\Delta_{net}\theta\right|_{\max}$ decreases as the semi-soft coefficient a increases.

To establish a relation between the maximal spontaneous strain $E^S_{\max}$ and the maximal net director rotation $\left|\Delta_{net}\theta\right|_{\max}(\varepsilon_0)$, we need to make use of the coupling constant $D_2 = r - 1/r + a$, which depends on the two material parameters r and a, as listed in Table 1. Fig. 11(d) depicts that at strains ε_0 up to 10%, $E^S_{\max}(\varepsilon_0)/D_2$ is bigger for samples with bigger $\left|\Delta_{net}\theta\right|_{\max}(\varepsilon_0)$. As shown by Fig. 11(e), $E^S_{\max}/D_2$ is an increasing function of ε_0, and decreases as the semi-soft coefficient a increases for strains ε_0 less than 10%. Note that the material constant $D_2 = r - 1/r + a$ represents the coupling between the spontaneous strain and the director rotation as first introduced by de Gennes (de Gennes, 1980), and discussed in details in the phenomenological theory for LCEs under small deformation by Warner and Terentjev (Warner and Terentjev, 2007). Thus, it is not surprising that the above results are well established at relatively small strains.

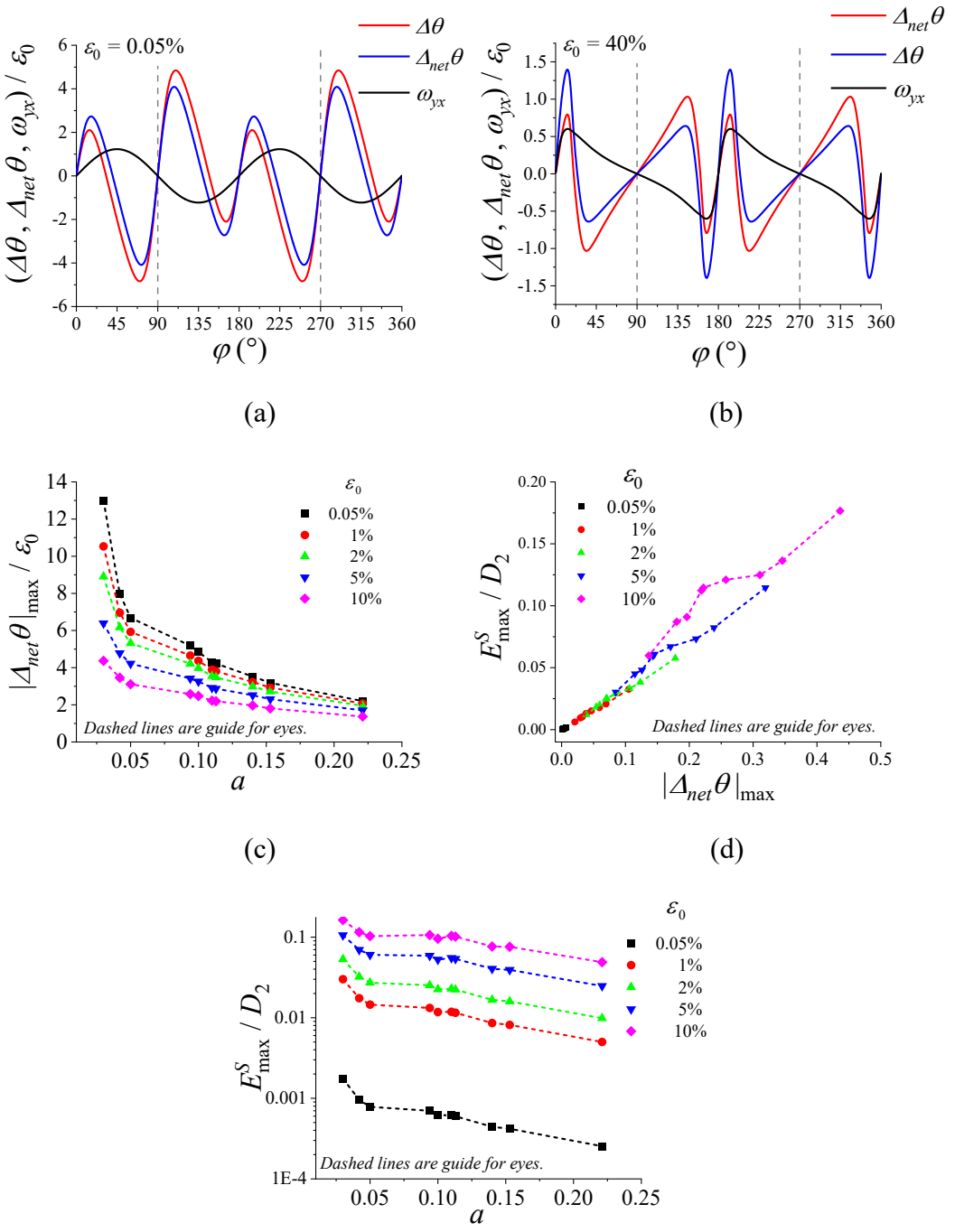

Fig. 11. The net rotation of the director, $\Delta_{net}\theta := \Delta\theta - \omega_{yx}$, and its effect on the spontaneous strains. (a) and (b) Distributions of the director rotation $\Delta\theta$, the rigid body rotation ω_{yx} and the net rotation $\Delta_{net}\theta$ on the hole edge at a small ($\varepsilon_0 = 0.05\%$) and a large ($\varepsilon_0 = 40\%$) prescribed strain for the deep nematic example (DNE). (c) the maximal net director rotation scaled by ε_0, $|\Delta_{net}\theta|_{\max} / \varepsilon_0$ and (e) the maximal spontaneous strain scaled by the coupling constant, $E^S_{\max} / D_2$ vs. a at prescribed ε_0. (d) the ratio $E^S_{\max} / D_2$ vs. $|\Delta_{net}\theta|_{\max}$ at the same ε_0. (The dashed lines are guide for the eyes, and the coupling constant $D_2 = r - 1/r + a$ is a material constant.)

Now, we are back to analyze the stress concentration factor. The stress concentration factor difference between a LCE sample and a n-H sample, $\Delta K_\sigma(\varepsilon_0) := K_\sigma^{LCE}(\varepsilon_0) - K_\sigma^{nH}(\varepsilon_0)$, always increases monotonically with the maximal spontaneous strain $E^S_{\max}(\varepsilon_0)$, as shown in Fig. 12(a). Thus, we can scale the stress concentration factor difference by the coupling constant D_2, and show that $\Delta K_\sigma(\varepsilon_0)/D_2$ increases with the maximal net director rotation $|\Delta_{net}\theta|_{\max}(\varepsilon_0)$ and decreases with the semi-soft coefficient a, as shown in Fig. 12(b) and (c).

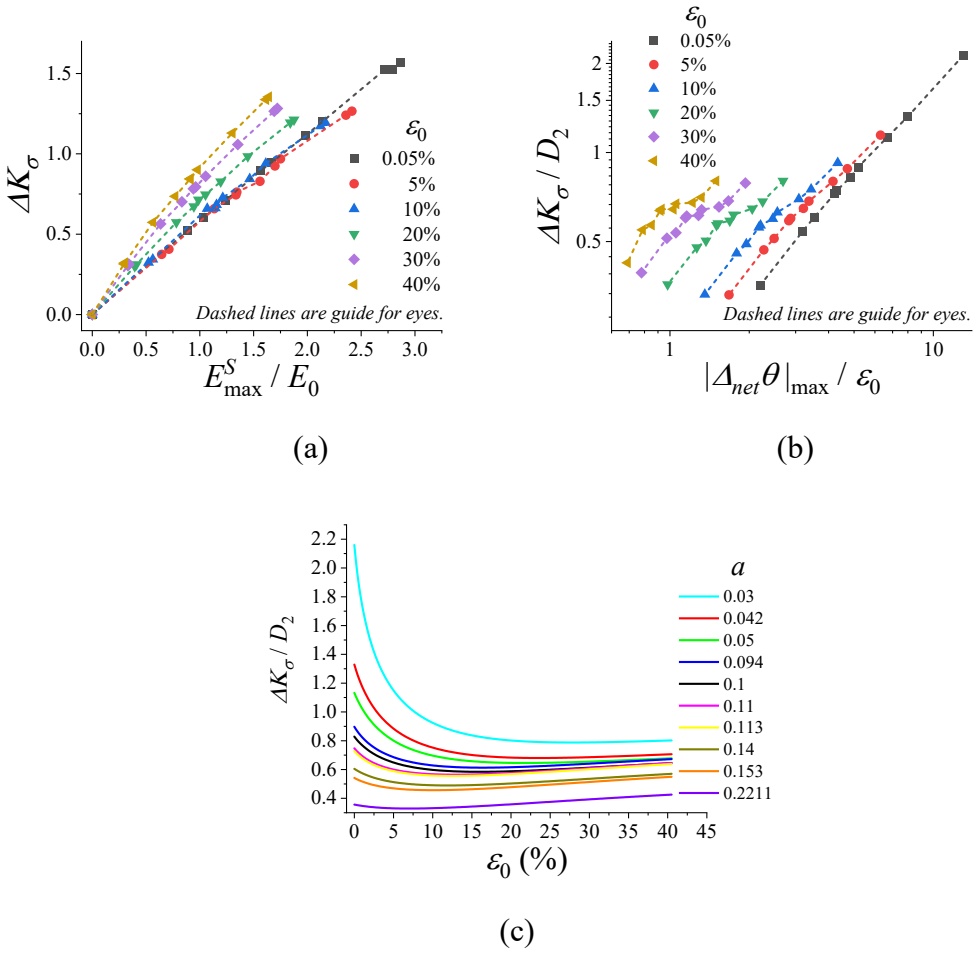

Fig. 12. The stress concentration factor difference between a LCE sample and a neo-Hookean material, $\Delta K_\sigma := K_\sigma^{LCE} - K_\sigma^{nH}$, and the effect of the spontaneous strains and the net director rotations for 10 LCE samples. (a) ΔK_σ vs. $E^S_{\max}/E_0$ and (b) $\Delta K_\sigma / D_2$ vs. $|\Delta_{net}\theta|_{\max}/\varepsilon_0$ at prescribed strain ε_0. The dashed lines are guide for eyes and $E_0 = (\lambda^2 - 1)/2$. (c) ΔK_σ vs. ε_0 for the 10 samples studied.

Similarly, the strain concentration factor difference $\Delta K_E(\varepsilon_0) \coloneqq K_E^{LCE}(\varepsilon_0) - K_E^{nH}(\varepsilon_0)$ increases monotonically with $E^S_{\max}(\varepsilon_0)$, as shown in Fig. 13(a). Among different samples with different r and a, the scaled factor difference $\Delta K_E(\varepsilon_0)/D_2$ mostly increases with $|\Delta_{net}\theta|_{\max}(\varepsilon_0)$, and $\Delta K_E/D_2$ is also mostly larger for samples with smaller semi-soft coefficient a at least small strains ($\varepsilon_0 < 5\%$), as shown in Fig. 13(b) and (c). Fig. 13(d) and (e) depict that the three possible scenarios observed previously for the concentration locations of the strain, $\varphi_E^M(\varepsilon_0)$ or the difference, $\Delta\varphi_E^M(\varepsilon_0) \coloneqq \left|\varphi_E^M(\varepsilon_0) - 90^\circ\right|$ correspond to different ranges of $E^S_{\max}/E_0$. Namely, when $E^S_{\max}/E_0$ is small ($E^S_{\max}/E_0 \le 1$), we would have $\varphi_E^M(\varepsilon_0) \equiv \varphi_\sigma^M = \pm 90^\circ$. When $1 < E^S_{\max}/E_0 \le 2$, we observe that $\Delta\varphi_E^M(\varepsilon_0)$ is nonzero at small ε_0 and decreases monotonically to zero with ε_0. For even larger $E^S_{\max}/E_0 > 2$, $\Delta\varphi_E^M(\varepsilon_0)$ is nonzero at small ε_0, and is non-monotonic before decreasing to zero.

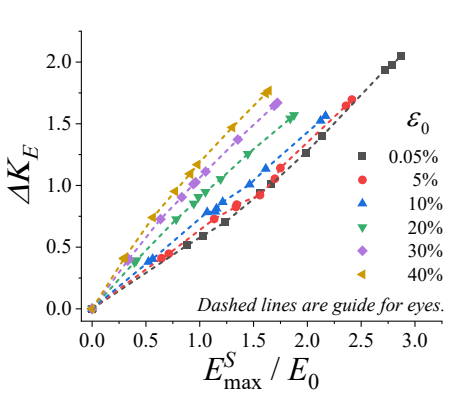

(a)

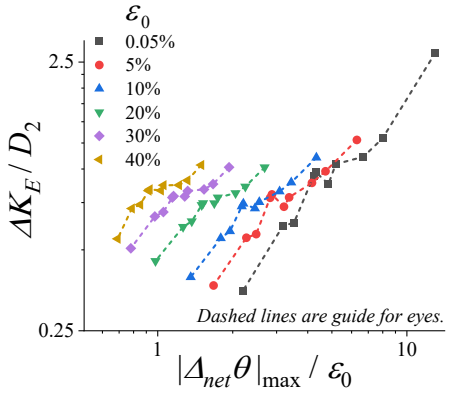

(b)

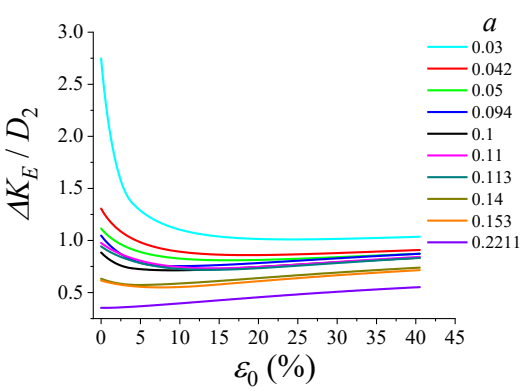

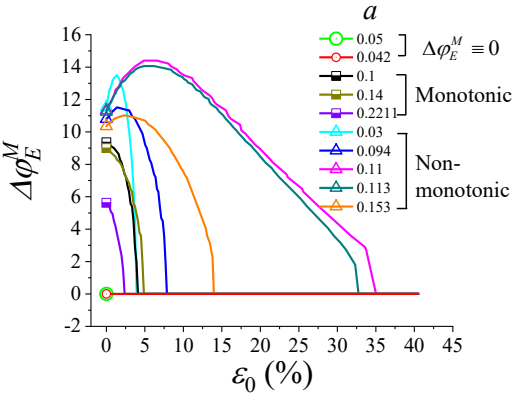

(c) (d)

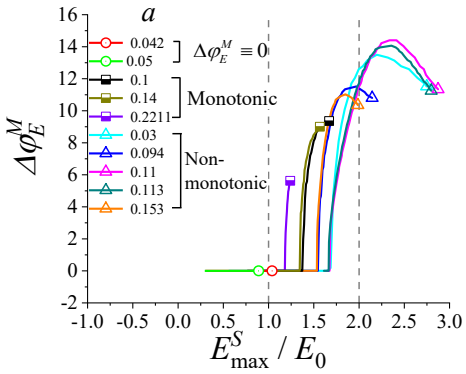

(e)

Fig. 13. The strain concentration factor difference between a LCE sample and a neo-Hookean material, $\Delta K_E := K_E^{LCE} - K_E^{NH}$, and the effect of the spontaneous strains and the net director rotations for 10 LCE samples. (a) ΔK_E vs $E^S_{\max}$ and (b) $\Delta K_E / D_2$ vs. $\left|\Delta_{net}\theta\right|_{\max} / \varepsilon_0$ at prescribed strains ε_0. The dashed lines are guide for the eyes and $E_0 = \left(\lambda^2 - 1\right)/2$. (c) $\Delta K_E / D_2$ and (d) the difference of the strain and stress concentration locations, $\Delta\varphi_E^M := \left|\varphi_E^M - 90°\right|$ vs. ε_0 for the 10 LCE samples studied. (e) $\Delta\varphi_E^M$ vs. $E^S_{\max} / E_0$.

5. Conclusions

The stress and strain concentration behaviors of a thin LCE sheet with a small circular hole are studied numerically by using the semi-soft elastic free energy. The results have shown clearly that the concentration behavior under uniaxial loading are generally very different from regular rubbers. And the unusual behavior of LCEs should be attributed to the stress induced director rotations near the edge of the center hole, where the stress state is quite different from the rest of the thin sheet under the uniaxial loading.

Comparing to the n-H material, we have observed a stronger stress concentration at the upper and lower middle points of the circular hole in a LCE sample. At the same time, the stress level and the free energy of the LCE are slightly lower under a prescribed external strain. Director rotations take place around the edge of the hole, resulting in a lower soft elastic energy but a higher semi-soft energy.

The director rotations have a much stronger effect on the strain concentration

behavior of LCEs than the n-H material due to the large spontaneous strains. Firstly, the strain concentration factor K_E of LCEs is not only much larger than the n-H material, but also varies non-monotonically with the loading. More interestingly, we have found that the locations of the strain and the stress concentrations do not coincide with each other, at least when the loading is not very large. In other words, there can be four strain concentration locations on the edge of the holes in contrast to two locations (the upper and lower middle points) for the stress concentration. We know that the total strain of a LCE sample is composed of the elastic and the spontaneous strains. While the elastic part is directly related to the stress distribution and has its maximum at the locations of the stress concentration, the spontaneous part is induced by the director rotations, which is determined by the distributions of the stress and the director alignment. Namely, we know from the uniaxial loading experiments of monodomain LCE samples that the director should rotate to align with the loading, i.e. the direction of the first principal stress. As the initial director of the LCE sheet is aligned along the loading axis, no rotation is needed in the sample except in a narrow region around the hole, where the stress is not uniaxial due to the free boundary condition. Thus, on the edge of the hole in the middle of a LCE sheet under uniaxial loadings, we observe stress and strain concentrations, and highly non-uniform director rotation and spontaneous strain. In particularly, at the locations of the stress concentration, the initial director is already tangent to the edge, so it will not rotate at all. Thus, the locations of the maximal director rotation and consequently the maximal spontaneous strain are always far away from the locations of the stress concentration. As a result, when the loading is not big enough, the spontaneous strain can make the locations of the total strain concentration deviate from its elastic part.

By considering monodomain LCE samples that are made of different materials and by different preparation methods as reported in some previous experiments, we have observed qualitatively similar stress/strain concentration behavior with

quantitatively different dependence on the two material parameters, r and a, which are the step length ratio reflecting the backbone anisotropy and the semi-soft coefficient, respectively. We have observed almost linear dependences between the stress/strain concentration factors and the maximal spontaneous strains for all the 10 samples studied. The maximal net director rotations are found to be larger for samples with smaller semi-soft coefficient a. The scaled stress concentration factor difference by a coupling constant that combines the effect of the two material parameters, r and a, increases as the semi-soft coefficient a decreases. Similar results are found for the scaled maximal spontaneous strains and the scaled strain concentration factor difference at small strains.

In addition, it should be noticed that our conclusions in this article might merely apply for relatively small and moderate loadings. As loading grows, the stress around the hole edge will approach the lock-up stretch, and the stress/strain concentration behaviors then might be more complicated and interesting, which is worth some further study. Two issues should be considered more carefully at large loadings, mesh convergence near the hole edge and the relevant hyperelastic models. Remeshing might be needed to ensure the numerical accuracy at very large deformations. Rubber elastic models considering the lock-up effect such as the Gent model should be employed.

Acknowledgement

Y.J. and Y.H. gratefully acknowledge the support of the National Natural Science Foundation of China (Grant Nos.: 12072077, 11772094 and 11872150). L.J. gratefully acknowledge the support of the National Science Foundation (Grant No. CMMI-1925790).

References

Biggins, J.S., Terentjev, E.M., Warner, M., 2008. Semisoft elastic response of nematic elastomers to complex deformations. Physical Review E 78, 041704.

Bladon, P., Terentjev, E.M., Warner, M., 1993. Transitions and instabilities in liquid crystal elastomers. Physical Review E 47, R3838-R3840.

Camacho-Lopez, M., Finkelmann, H., Palffy-Muhoray, P., Shelley, M., 2004. Fast

liquid-crystal elastomer swims into the dark. Nature Materials 3, 307-310.

Conti, S., 2002. Soft elastic response of stretched sheets of nematic elastomers: a numerical study. Journal of the Mechanics and Physics of Solids 50, 1431-1451.

Conti, S., DeSimone, A., Dolzmann, G., 2002. Semisoft elasticity and director reorientation in stretched sheets of nematic elastomers. Physical Review E 66, 061710.

Davidson, Z.S., Shahsavan, H., Aghakhani, A., Guo, Y., Hines, L., Xia, Y., Yang, S., Sitti, M., 2019. Monolithic shape-programmable dielectric liquid crystal elastomer actuators. Science Advances 5, eaay0855.

de Gennes, P.G., 1980. Weak Nematic Gels, in: Helfrich, W., Heppke, G. (Eds.), Liquid Crystals of One- and Two-Dimensional Order and Their Applications. Springer-Verlag Berlin Heidelberg 1980, Garmisch-Partenkirchen, Fed. Rep. of Germany, pp. 231-237.

de Gennes, P.G., Prost, J.P., 1994. The Physics of Liquid Crystals. Oxford University Press, Oxford.

Dey, S., Agra-Kooijman, D., Ren, W., McMullan, P., Griffin, A., Kumar, S., 2013. Soft elasticity in main chain liquid crystal elastomers. Crystals 3, 363-390.

Elmukashfi, E., Kroon, M., 2014. Numerical analysis of dynamic crack propagation in biaxially strained rubber sheets. Engineering Fracture Mechanics 124-125, 1-17.

Fan, W., Wang, Z., Cai, S., 2016. Rupture of polydomain and monodomain liquid crystal elastomer. International Journal of Applied Mechanics 08, 164001.

Finkelmann, H., Greve, A., Warner, M., 2001a. The elastic anisotropy of nematic elastomers. European Physical Journal E 5, 281-293.

Finkelmann, H., Kundler, I., Terentjev, E.M., Warner, M., 1997. Critical stripe-domain instability of nematic elastomers. Journal De Physique Ii 7, 1059-1069.

Finkelmann, H., Nishikawa, E., Pereira, G.G., Warner, M., 2001b. A new opto-mechanical effect in solids. Physical Review Letters 87, 015501.

Fowler, G.F., 1984. Finite plane and anti-plane elastostatic fields with discontinuous deformation gradients near the tip of a crack. Journal of Elasticity 14, 287-328.

Fukahori, Y., Seki, W., 1993a. Stress analysis of elastomeric materials at large extensions using the finite element method. Journal of Materials Science 28, 4143-4152.

Fukahori, Y., Seki, W., 1993b. Stress analysis of elastomeric materials at large extensions using the finite element method. Journal of Materials Science 28, 4471-4482.

Fukunaga, A., Urayama, K., Takigawa, T., DeSimone, A., Teresi, L., 2008. Dynamics of electro-opto-mechanical effects in swollen nematic elastomers. Macromolecules 41, 9389-9396.

Gebhart, S.C., Thompson, R.C., Mahadevan-Jansen, A., 2007. Liquid-crystal tunable filter spectral imaging for brain tumor demarcation. Applied Optics 46, 1896-1910.

Gomes, C.J., Troyani, N., Morillo, C., Gregory, S., Gerardo, V., Pollonais, Y., 2005. Theoretical stress concentration factors for short flat tension bars with opposite U-shaped notches. The Journal of Strain Analysis for Engineering Design 40, 345-355.

He, X., Zheng, Y., He, Q., Cai, S., 2020. Uniaxial tension of a nematic elastomer with inclined mesogens. Extreme Mechanics Letters 40, 100936.

Heydari-Meybodi, M., Ayatollahi, M.R., Berto, F., 2018. Rupture analysis of rubber in the presence of a sharp V-shape notch under pure mode-I loading. International Journal of Mechanical Sciences 146-147, 405-415.

Higaki, H., Takigawa, T., Urayama, K., 2013. Nonuniform and Uniform Deformations of Stretched Nematic Elastomers. Macromolecules 46, 5223-5231.

Hirschmann, H., Roberts, P.M.S., Davis, F.J., Guo, W., Hasson, C.D., Mitchell, G.R., 2001. Liquid crystalline elastomers: the relationship between macroscopic behaviour and the level of backbone anisotropy. Polymer 42, 7063-7071.

Jin, L., Zeng, Z., Huo, Y., 2010. Thermomechanical modeling of the thermo-order–mechanical coupling behaviors in liquid crystal elastomers. Journal of the Mechanics and Physics of Solids 58, 1907-1927.

Khajehsaeid, H., Reese, S., Arghavani, J., Naghdabadi, R., 2016. Strain and stress

concentrations in elastomers at finite deformations: effects of strain-induced crystallization, filler reinforcement, and deformation rate. Acta Mechanica 227, 1969-1982.

Kuenstler, A.S., Chen, Y., Bui, P., Kim, H., DeSimone, A., Jin, L., Hayward, R.C., 2020. Blueprinting photothermal shape-morphing of liquid crystal elastomers. Advanced Materials 32, e2000609.

Kundler, I., Finkelmann, H., 1995. Strain-induced director reorientation in nematic liquid single crystal elastomers. Macromolecular Rapid Communications 16, 679-686.

Küpfer, J., Finkelmann, H., 1994. Liquid crystal elastomers: Influence of the orientational distribution of the crosslinks on the phase behaviour and reorientation processes. Macromolecular Chemistry and Physics 195, 1353-1367.

Larocca, N.M., Hage, E., Pessan, L.A., 2004. Toughening of poly(butylene terephthalate) by AES terpolymer. Polymer 45, 5265-5277.

Legrain, G., Moës, N., Verron, E., 2005. Stress analysis around crack tips in finite strain problems using the eXtended finite element method. International Journal for Numerical Methods in Engineering 63, 290-314.

Lindley, P.B., 1971. Plane-stress analysis of rubber at high strains using finite elements. Journal of Strain Analysis 6, 45-52.

Lindley, P.B., 2007. Strain concentrations at the corners of stretched rubber sheets. Journal of Strain Analysis 6, 279-285.

Livne, A., Bouchbinder, E., Fineberg, J., 2008. Breakdown of linear elastic fracture mechanics near the tip of a rapid crack. Physical Review Letters 101, 264301.

Mitchell, G.R., Davis, F.J., Guo, W., 1993. Strain-induced transitions in liquid-crystal elastomers. Physical Review Letters 71, 2947-2950.

Petelin, A., Copic, M., 2010. Strain dependence of the nematic fluctuation relaxation in liquid-crystal elastomers. Physical Review E 82, 011703.

Plucinsky, P., Bhattacharya, K., 2017. Microstructure-enabled control of wrinkling in nematic elastomer sheets. Journal of the Mechanics and Physics of Solids 102, 125-150.

Qian, H.S., Gao, Y.C., 2001. Large deformation character of two kinds of models for rubber. International Journal of Engineering Science 39, 39-51.

Rivlin, R.S., Thomas, A.G., 1951. Large elastic deformations of isotropic materials. VIII. Strain Distribution around a Hole in a Sheet. Philosophical Transactions of the Royal Society of London. Series A, Mathematical and Physical Sciences 243, 289-298.

Roberts, P.M.S., Mitchell, G.R., Davis, F.J., 1997. A single director switching mode for monodomain liquid crystal elastomers. Journal De Physique Ii 7, 1337-1351.

Sawa, Y., Urayama, K., Takigawa, T., DeSimone, A., Teresi, L., 2010. Thermally driven giant bending of liquid crystal elastomer films with hybrid alignment. Macromolecules 43, 4362-4369.

Schuhladen, S., Preller, F., Rix, R., Petsch, S., Zentel, R., Zappe, H., 2014. Iris-Like Tunable Aperture Employing Liquid-Crystal Elastomers. Advanced Materials 26, 7247-7251.

Spagnoli, A., Terzano, M., Brighenti, R., Artoni, F., Carpinteri, A., 2019. How Soft Polymers Cope with Cracks and Notches. Applied Sciences 9, 1086.

Tajbakhsh, A.R., Terentjev, E.M., 2001. Spontaneous thermal expansion of nematic elastomers. European Physical Journal E 6, 181-188.

Thomsen, D.L., Keller, P., Naciri, J., Pink, R., Jeon, H., Shenoy, D., Ratna, B.R., 2001. Liquid crystal elastomers with mechanical properties of a muscle. Macromolecules 34, 5868-5875.

Troyani, N., 2003. Simultaneous considerations of length and boundary conditions on theoretical stress concentration factors. International Journal of Fatigue 25, 353-355.

Troyani, N., Gomes, C., Sterlacci, G., 2002. Theoretical stress concentration factors for short rectangular plates with centered circular holes. Journal of Mechanical Design 124, 126-128.

Tsui, C.P., Tang, C.Y., Lee, T.C., 2001. Finite element analysis of polymer composites filled by interphase coated particles. Journal of Materials Processing

Technology 117, 105-110.

Verwey, G.C., Warner, M., 1995. Soft Rubber Elasticity. Macromolecules 28, 4303-4306.

Verwey, G.C., Warner, M., 1997. Compositional Fluctuations and Semisoftness in Nematic Elastomers. Macromolecules 30, 4189-4195.

Verwey, G.C., Warner, M., Terentjev, E.M., 1996. Elastic Instability and Stripe Domains in Liquid Crystalline Elastomers. Journal De Physique Ii 6, 1273-1290.

Walter, D.P., Deborah, F., 2007. Peterson's stress concentration factors, 3rd Edition ed. John Wiley& Sons, Hoboken, New Jersey.

Wang, Q.Z., Lee, D.J., 1999. Predictive modelling for rubber-toughened polymers. Mechanics of Materials 31, 705-716.

Wang, Z., Fan, W., He, Q., Wang, Y., Liang, X., Cai, S., 2017. A simple and robust way towards reversible mechanochromism: Using liquid crystal elastomer as a mask. Extreme Mechanics Letters 11, 42-48.

Warner, M., 1999. New elastic behaviour arising from the unusual constitutive relation of nematic solids. Journal of the Mechanics and Physics of Solids 47, 1355-1377.

Warner, M., Terentjev, E.M., 1996. Nematic elastomers—A new state of matter? Progress in Polymer Science 21, 853-891.

Warner, M., Terentjev, E.M., 2007. Liquid Crystal Elastomers, Clarendon Press, Oxford.

Woltman, S.J., Jay, G.D., Crawford, G.P., 2007. Liquid-crystal materials find a new order in biomedical applications. Nature Materials 6, 929-938.

Wong, F.S., Shield, R.T., 1969. Large plane deformations of thin elastic sheets of neo-Hookean material. Zeitschrift für angewandte Mathematik und Physik ZAMP 20, 176-199.

Xing, H.H., Li, J., Shi, Y., Guo, J.B., Wei, J., 2016. Thermally Driven Photonic Actuator Based on Silica Opal Photonic Crystal with Liquid Crystal Elastomer. Acs Applied Materials & Interfaces 8, 9440-9445.

Yang, W.H., 1967. Stress Concentration in a Rubber Sheet Under Axially Symmetric Stretching. Journal of Applied Mechanics 34, 942-946.

Yang, Z., 2009. Stress and strain concentration factors for tension bars of circular cross-section with semicircular groove. Engineering Fracture Mechanics 76, 1683-1690.

Yang, Z., Kim, C.-B., Cho, C., Beom, H.G., 2008. The concentration of stress and strain in finite thickness elastic plate containing a circular hole. International Journal of Solids and Structures 45, 713-731.

Zentel, R., 1986. Shape variation of cross-linked liquid-crystalline polymers by electric fields. Liquid Crystals 1, 589-592.

Zhang, Y., Xuan, C., Jiang, Y., Huo, Y., 2019. Continuum mechanical modeling of liquid crystal elastomers as dissipative ordered solids. Journal of the Mechanics and Physics of Solids 126, 285-303.

Zhang, Y., Zhang, Z., Huo, Y., 2020. Nucleation and critical conditions for stripe domains in monodomain nematic elastomer sheets under uniaxial loading. Journal of the Mechanics and Physics of Solids 144(2020), 104110.

Zubarev, E.R., Kuptsov, S.A., Yuranova, T.I., Talroze, R.V., Finkelmann, H., 1999. Monodomain liquid crystalline networks: reorientation mechanism from uniform to stripe domains. Liquid Crystals 26, 1531-1540.